

Photoelectric Emission from Interstellar Dust: Grain Recoil Forces and Gas Heating

Joseph C. Weingartner

Physics Dept., Jadwin Hall, Princeton University, Princeton, NJ 08544, USA;
josephw@astro.princeton.edu

and

B.T. Draine

Princeton University Observatory, Peyton Hall, Princeton, NJ 08544, USA;
draine@astro.princeton.edu

ABSTRACT

Interstellar grains exposed to anisotropic radiation are subjected to forces due to recoil from escaping photoelectrons. This “photoelectric” force, which depends on grain charge and therefore on ambient conditions, can exceed the direct “radiation pressure” force due to scattering and absorption of photons. The photoemissive recoil force is estimated as a function of grain size for graphite and silicate grains, for various interstellar environments. The anisotropy of the radiation field in the solar neighborhood is estimated, and used to estimate gas-grain drift speeds in various environments. Photoelectric heating efficiencies are presented as a function of grain size. We construct grain size distributions for which there is substantial mass in very small graphite grains and which are consistent with the observed average extinction for lines of sight with $R_V = 3.1$, 4.0, and 5.5. The net gas heating rate is evaluated for each of these size distributions.

Subject headings: dust

1. Introduction

It has long been recognized that photoelectric emission from dust grains can be an important mechanism for heating interstellar gas (Watson 1972; de Jong 1977; Draine 1978; Tielens & Hollenbach 1985; Bakes & Tielens 1994). Lafon (1990) noted that this process

could be important for grain dynamics as well, when the incident radiation is unidirectional. Lafon (1990) considered spherical grains, and assumed that electrons are emitted only from the illuminated hemisphere. He found that, under some interstellar conditions, the resulting recoil force on the grain substantially exceeds the force due to the usual radiation pressure. However, interstellar grain radii can be smaller than the photon attenuation length, so electrons are also emitted from the non-illuminated hemisphere. Thus, we revisit the calculation of photoemissive recoil forces on dust grains, employing the prescription of Kerker & Wang (1982) for estimating the anisotropy in photoelectron momentum. We consider both silicate and carbonaceous grains; for small carbonaceous particles we use photoelectric yields as estimated by Bakes & Tielens (1994).

In §2 we discuss our adopted model for photoelectric emission from grains, in §3 we characterize the relevant ambient conditions, and in §4 we evaluate the photoelectric recoil force as a function of grain size. The recoil force depends on the anisotropy of the radiation field, so in §5 we use star counts to discuss the starlight anisotropy in the solar neighborhood. In §6 we estimate the resulting gas-grain drift speeds for various interstellar environments. We consider potential consequences of gas-grain drift in §7, including grain-grain collisions. We adopt a grain size distribution which contains a substantial population of very small grains (with sizes $\lesssim 30 \text{ \AA}$) but is consistent with observed extinction as a function of wavelength; we discuss grain size distributions in Appendix A. In §8 we calculate photoelectric gas heating rates as a function of grain size and integrate them over the distributions obtained in Appendix A. We briefly summarize our results in §9.

2. Photoelectric Emission from Grains

2.1. Photoelectric Yields

Consider a spherical graphite or silicate grain illuminated by a unidirectional radiation field. Some fraction of the photon absorptions will result in the ejection of an electron. We do not attempt a theoretical calculation of this yield from first principles. Draine (1978) displayed yield measurements from experiments on bulk samples of materials of interest, including graphite, lunar dust, and silicon carbide. Watson (1972, 1973) pointed out that the yields of submicron particles are expected to be enhanced relative to the bulk yields, because of the finite electron escape length. An electron excited somewhere in the volume of the sample can lose energy during its journey to the surface, through interactions with electrons and with phonons. The result is that the fraction of electrons which escape energy loss goes roughly as $\exp(-x/l_e)$, where x is the distance the electron has traveled and l_e is the “electron escape length.” Generally, the photon attenuation length, l_a (equal to the

e -folding length for the decrease in radiation intensity as it propagates into the material), exceeds l_e , and the electrons excited deep inside a bulk sample do not reach the surface. Small grain sizes limit the distance from electron excitation to surface, so the yield is enhanced.

Apparently there are other considerations affecting the yield enhancement besides the above geometrical effect. A series of experiments (Schmidt-Ott et al. 1980; Burtscher & Schmidt-Ott 1982; Burtscher et al. 1984; Müller et al. 1988) on free silver spheres with radii between 27 and 54 Å found yield enhancements in excess of expectations by factors of several. A later theoretical effort (Faraci, Pennisi, & Margaritondo 1989) was able to reproduce the results, but only by assuming that the condition for an electron to escape, when incident on the surface from within, depends only on its energy and not on its direction of motion. The estimates adopted here for size-dependent yields from grains, which include only a simple correction for the geometrical effect, must be regarded as provisional. Reliable calculations of effects involving photoelectric emission from interstellar dust will not be possible until experiments have been performed on submicron grains of appropriate composition.

The ionization potential, IP , is another quantity in photoemission which depends on grain size. The best understood effect is the change in electrostatic energy resulting from the removal of an electron. Although other shifts, related to changes in band structure with particle size, might be significant (see, e.g., §7 of the review by Nagaev 1992), it is unclear how to compute them, so we will follow Bakes & Tielens (1994) in considering only the electrostatic term. We assume that photoelectrons do not tunnel across the Coulomb barrier for negatively-charged grains, implying $IP = w$. Thus,

$$IP = \begin{cases} w + \left(Z + \frac{1}{2}\right) e^2/a & , Z \geq 0 \\ w & , Z < 0 \end{cases} , \quad (1)$$

where w is the bulk work function, Z is the grain charge in units of the proton charge e , and a is the grain radius.

We adopt the following, physically motivated, expression for the yield:

$$Y(h\nu, IP, a) = \min [y_0(h\nu)y_1(IP, h\nu)y_2(a, h\nu), 1] . \quad (2)$$

Here $y_0(h\nu)$ is the yield as a function of photon energy $h\nu$ for uncharged bulk material, $y_1(IP, h\nu)$ is the factor by which the yield changes when $IP > w$, and $y_2(a, h\nu)$ is the factor by which the yield for a grain with radius a is enhanced over that of bulk material; y_2 depends on $h\nu$ because l_a does.

Draine (1978) found that the following estimate for y_2 reproduces Watson's (1973)

detailed results based on Mie theory, to within 20%:

$$y_2 = \left(\frac{\beta}{\alpha}\right)^2 \frac{\alpha^2 - 2\alpha + 2 - 2\exp(-\alpha)}{\beta^2 - 2\beta + 2 - 2\exp(-\beta)}, \quad (3)$$

where $\beta = a/l_a$ and $\alpha = a/l_a + a/l_e$.

Electron escape lengths for most materials reach a minimum in the vicinity of tens of eV and increase at higher and lower energies. The data are meager for electron energies below 10 eV, but Martin et al. (1987) found, for thin carbon films, that l_e fell into a broad minimum of 6 Å around 40 eV and rose to 9 Å at 6 eV. McFeely et al. (1990) found, for SiO₂, that l_e varied from 5.7 to 6.8 Å for electron energies between 8 and 20 eV, and one might expect similar values for silicates. Bakes & Tielens (1994) assumed $l_e = 10$ Å, independent of energy, and we use the same value here, for both graphite and silicates.

The photon attenuation length is given by

$$l_a = \frac{\lambda}{4\pi\text{Im}(m)}, \quad (4)$$

where λ is the wavelength in vacuo and $m(\lambda)$ is the complex refractive index. Graphite is a highly anisotropic material, so that the dielectric function is a tensor. This tensor may be diagonalized by choosing Cartesian coordinates with two of the axes lying in the “basal” plane; the third axis, normal to the basal plane, is called the “*c*-axis”. For graphite, we take

$$l_a^{-1} = \frac{4\pi}{\lambda} \left(\frac{2}{3}\text{Im}(m_{\perp}) + \frac{1}{3}\text{Im}(m_{\parallel}) \right), \quad (5)$$

where m_{\perp} and m_{\parallel} are for the electric field perpendicular and parallel to the *c*-axis, respectively. In computing l_a , we use dielectric functions from Draine & Lee (1984) and Laor & Draine (1993).

When $IP > w$, photoelectrons which are emitted with an initial kinetic energy $E < IP - w$ return to the grain rather than escaping to infinity, decreasing the yield. Thus,

$$y_1(IP, h\nu) = \int_{IP-w}^{h\nu-w} f_E(E) dE, \quad (6)$$

where $f_E(E)dE$ gives the fraction of photoelectrons with initial kinetic energy between E and $E + dE$. We adopt a parabolic distribution for E :

$$f_E = \frac{6E(h\nu - w - E)}{(h\nu - w)^3}, \quad (7)$$

which implies

$$y_1(IP, h\nu) = 1 + \left(\frac{IP - w}{h\nu - w}\right)^2 \left[2 \left(\frac{IP - w}{h\nu - w}\right) - 3 \right]. \quad (8)$$

At present, the bulk yields for grain materials are unknown. Draine (1978) shows, in his Figure 1, that the yields for graphite measured by Feuerbacher & Fitton (1972) are unusually low, and lie more than an order of magnitude below the yields for anthracene (Fujihira, Hirooka, & Inokuchi 1973). Bakes & Tielens (1994) chose a bulk yield function such that the resulting yield for grains with $a = 4 \text{ \AA}$ would approximately reproduce the photoionization yield for coronene, as measured by Verstraete et al. (1990). We adopt a similar approach, and take

$$y_0(h\nu) = \frac{7 \times 10^{-3} \left(\frac{h\nu}{w} - 1 \right)^5}{1 + 3.7 \times 10^{-2} \left(\frac{h\nu}{w} - 1 \right)^5}, \quad (9)$$

with $w = 4.4 \text{ eV}$. It is important to note that our $y_0(h\nu)$ substantially exceeds the measured yields for bulk graphite¹. This apparent inconsistency could imply one or more of the following: 1. The yield for bulk graphite differs substantially from that for bulk coronene. 2. The measured yields for bulk graphite are wrong. 3. Our prescription for $y_2(a, h\nu)$ is wrong. Clearly, the adopted yields for graphite grains are highly uncertain.

The situation for silicates is no better. Feuerbacher et al. (1972) measured the yield for a powdered sample of lunar dust, and found that Y decreases rapidly as photon energy is decreased below 14 eV . However, they noted that the use of the powdered sample might result in yields that are too low. Thus, we adopt a yield for silicates which somewhat exceeds the results of Feuerbacher et al. at 14 eV , but which does not drop as rapidly for lower values of $h\nu$:

$$y_0(h\nu) = \frac{0.5 \left(\frac{h\nu}{w} - 1 \right)}{1 + 5 \left(\frac{h\nu}{w} - 1 \right)}, \quad (10)$$

with $w = 8 \text{ eV}$. We have also computed the photoelectric force and heating efficiency for an alternate (“low-yield”) silicate yield function which reproduces the low yields of Feuerbacher et al.; the results are generally smaller by less than a factor of 2.

In Figure 1 we plot $Y(h\nu)$ for neutral graphite and silicate grains of several sizes; we also show the low-yield silicate y_0 .

¹For example, at $h\nu = 10 \text{ eV}$, equation (9) gives $y_0 = 2.1 \times 10^{-2}$, whereas Feuerbacher & Fitton (1972) report a yield of only 8×10^{-3} at this energy.

2.2. Grain Charging

Since the photoemission depends on the ionization potential, it is necessary to know the distribution of charge states for the grains. In statistical equilibrium,

$$f(Z)[J_{\text{pe}}(Z) + J_{\text{ion}}(Z)] = f(Z + 1)J_e(Z + 1), \quad (11)$$

where $f(Z)$ is the probability for the grain charge to be Ze , J_{pe} is the photoemission rate, J_{ion} is the positive ion accretion rate, and J_e is the electron accretion rate. Bakes & Tielens (1994) discuss the most positive and most negative charges that a grain could possibly acquire ($Z_{IP}e$ and $-Z_{EA}e$, respectively). The most positive charge is one proton charge more than the highest charge for which an electron can be ejected (i.e. for which $IP < 13.6 \text{ eV}$, in an H I region), and $-Z_{EA}e$ is the most negative charge for which $IP > 0$ (i.e. for which autoionization does not occur). Thus,

$$Z_{IP} = \text{int} \left[(13.6 \text{ eV} - w) \frac{a}{e^2} + \frac{1}{2} \right] \quad (12)$$

and

$$Z_{EA} = \text{int} \left[\frac{wa}{e^2} + \frac{1}{2} \right], \quad (13)$$

where $\text{int}[x]$ denotes the greatest integer less than x . By iteratively applying equation (11) and normalizing, f can be found for all Z .

The accretion rates are given by

$$J_i(Z) = n_i s_i \left(\frac{8kT}{\pi m_i} \right)^{1/2} \pi a^2 \tilde{J}, \quad (14)$$

where n_i is the number density of species i , s_i is the sticking coefficient for the species on the grain, m_i is the particle mass, T is the gas temperature, and \tilde{J} is a function of $\eta_i \equiv akT/q_i^2$ and $\xi_i \equiv Ze/q_i$ (q_i is the charge of species i and k is the Boltzmann constant). Expressions for \tilde{J} can be found in Draine & Sutin (1987). The photoemission rate is given by

$$J_{\text{pe}} = \pi a^2 \int_{\nu_Z}^{\nu_H} Y Q_{\text{abs}} \frac{cu_\nu}{h\nu} d\nu, \quad (15)$$

where $\nu_Z = IP/h$, $\nu_H = 13.6 \text{ eV}/h$, Q_{abs} is the absorption efficiency, u_ν is the radiation energy density per frequency interval, and c is the speed of light. Bakes & Tielens (1994) assumed $Q_{\text{abs}} \propto a$, valid for grains with $a \lesssim 100 \text{ \AA}$. Since we consider larger grains, we evaluate Q_{abs} using a Mie theory code derived from BHMIE (Bohren & Huffman 1983), with dielectric functions as described by Draine & Lee (1984) and Laor & Draine (1993). For graphite grains, we adopt the usual “1/3 – 2/3” approximation, and assume that $Q_{\text{abs}} = [Q_{\text{abs}}(\epsilon_{\parallel}) + 2Q_{\text{abs}}(\epsilon_{\perp})]/3$, where ϵ_{\parallel} and ϵ_{\perp} are the components of the graphite dielectric tensor for the electric field parallel and perpendicular to the c -axis, respectively.

3. Ambient Conditions

3.1. Radiation Fields

For most calculations, we adopt a blackbody spectrum for the radiation field, with color temperature T_c and dilution factor W , so that $u_\nu = 4\pi W B_\nu(T_c)/c$. It is convenient to characterize the radiation intensity by $G \equiv u_{\text{rad}}^{\text{uv}}/u_{\text{Hab}}^{\text{uv}}$, where $u_{\text{rad}}^{\text{uv}}$ is the energy density in the radiation field between 6 eV and 13.6 eV and $u_{\text{Hab}}^{\text{uv}} = 5.33 \times 10^{-14} \text{ erg cm}^{-3}$ is the Habing (1968) estimate of the starlight energy density in this range.² The radiation is cut off at 13.6 eV.

For the diffuse ISM, we adopt the average interstellar radiation field (ISRF) spectrum in the solar neighborhood, as estimated by Mezger, Mathis, & Panagia (1982) and Mathis, Mezger, & Panagia (1983):

$$\nu u_\nu^{\text{ISRF}} = \begin{cases} 0 & , h\nu > 13.6 \text{ eV} \\ 3.328 \times 10^{-9} \text{ erg cm}^{-3} \left(\frac{h\nu}{\text{eV}}\right)^{-4.4172} & , 11.2 \text{ eV} < h\nu < 13.6 \text{ eV} \\ 8.463 \times 10^{-13} \text{ erg cm}^{-3} \left(\frac{h\nu}{\text{eV}}\right)^{-1} & , 9.26 \text{ eV} < h\nu < 11.2 \text{ eV} \\ 2.055 \times 10^{-14} \text{ erg cm}^{-3} \left(\frac{h\nu}{\text{eV}}\right)^{0.6678} & , 5.04 \text{ eV} < h\nu < 9.26 \text{ eV} \\ \frac{4\pi\nu}{c} \sum_{i=1}^3 W_i B_\nu(T_i) & , h\nu < 5.04 \text{ eV} \end{cases} ; \quad (16)$$

the dilution factors and blackbody temperatures are given in Table 1. The total energy density in the ISRF of equation (16) is $u = 8.64 \times 10^{-13} \text{ erg cm}^{-3}$, with $u_{\text{rad}}^{\text{uv}} = 6.07 \times 10^{-14} \text{ erg cm}^{-3}$ in the 6-13.6 eV interval, or $G = 1.13$.

The spectrum-averaged efficiency factors for absorption and radiation pressure are

$$\langle Q_{\text{abs}} \rangle \equiv \frac{\int_0^{\nu_H} Q_{\text{abs}} u_\nu d\nu}{\int_0^{\nu_H} u_\nu d\nu}, \quad (17)$$

$$\langle Q_{\text{pr}} \rangle \equiv \frac{\int_0^{\nu_H} [Q_{\text{abs}} + Q_{\text{sca}}(1 - \langle \cos \theta \rangle)] u_\nu d\nu}{\int_0^{\nu_H} u_\nu d\nu}, \quad (18)$$

where $Q_{\text{abs}}\pi a^2$ is the absorption cross section, $Q_{\text{sca}}\pi a^2$ is the scattering cross section, and $\langle \cos \theta \rangle$ is the usual scattering asymmetry factor. In Figures 2 and 3 we display $\langle Q_{\text{abs}} \rangle$ and $\langle Q_{\text{pr}} \rangle$, respectively, for the ISRF and blackbody spectra with various values of T_c .

² For comparison, the interstellar radiation field estimated by Draine (1978) has $u = 8.93 \times 10^{-14} \text{ erg cm}^{-3}$ between 6 and 13.6 eV, or $G = 1.68$.

3.2. Scaling Law

The photoelectric emission is dependent on the ambient conditions, which can be characterized by the shape of the radiation spectrum, the gas temperature T , and one additional parameter, depending on the ratio G/n_e , which we take to be $G\sqrt{T}/n_e$.

Unless otherwise noted, we will display results for a blackbody spectrum with $T_c = 3 \times 10^4$ K, cut off at 13.6 eV. In Figure 4, the average electrostatic potential, $\langle U \rangle$, is plotted for two values of T , 100 K and 1000 K, and four values of $G\sqrt{T}/n_e$, ranging from 10^3 to 10^6 K^{1/2} cm³. We also provide results for conditions appropriate for the cold neutral medium (ISRF, $T = 100$ K, $n_e = 0.03$ cm⁻³, $G\sqrt{T}/n_e = 330$) and the warm neutral medium (ISRF, $T = 6000$ K, $n_e = 0.03$ cm⁻³, $G\sqrt{T}/n_e = 2600$). Note that for given $G\sqrt{T}/n_e$, the computed potentials show hardly any dependence on T .

To see why $G\sqrt{T}/n_e$ is a good parameter to describe grain charging, we make the approximation that the charge state on any grain remains constant, i.e.

$$J_e = J_{\text{pe}} + J_{\text{ion}}. \quad (19)$$

We neglect J_{ion} by virtue of the large proton mass and consider a positively charged grain with $U \sim 1$ V. The Draine & Sutin (1987) expression for \tilde{J} for a grain with static dielectric constant $\epsilon(0) \gg 1$ and $\xi_i < 0$ is

$$\tilde{J} \approx \left(1 - \frac{\xi_i}{\eta_i}\right) \left[1 + \left(\frac{2}{\eta_i - 2\xi_i}\right)^{1/2}\right], \quad (20)$$

which expands, for $eU/kT \gg 1$, to give

$$\tilde{J} \approx \frac{eU}{kT} (1 + Z^{-1/2}). \quad (21)$$

We express

$$J_{\text{pe}} \propto G \langle Q_{\text{abs}} \rangle a^2 g(U, a), \quad (22)$$

where $\langle Q_{\text{abs}} \rangle$ is the average value of Q_{abs} over the range of absorbed photon energies. Here $g(U, a)$ must be a decreasing function of U and g depends on a through the size dependence of the yield Y (see equations 2 and 3). Thus,

$$\frac{U (1 + Z^{-1/2})}{g(U, a)} \propto \langle Q_{\text{abs}} \rangle \frac{G\sqrt{T}}{n_e}. \quad (23)$$

Note that this result applies only when G/n_e is large enough (for given T and a) to keep the grains strongly positively charged (with $eU \gtrsim kT$). For low values of G/n_e , J_{ion}

plays a significant role in the grain charging. This introduces an additional dependence on the ionization fraction $x \equiv n_e/n_H$, since for the lowest x (i.e. $x \lesssim 2 \times 10^{-4}$), the ions are predominantly C^+ , whereas H^+ dominates for higher x , and J_{ion} depends on the ion mass. We assume H^+ in our calculations for the CNM and WNM and C^+ in our other calculations. For the values of $G\sqrt{T}/n_e$ and T considered here, the dependence on ion mix is only significant for the smallest grains, and even then extreme changes in the ion mix lead to only modest changes in the results. In Figure 5 we display $(G\sqrt{T}/n_e)_0$, the value of the charging parameter for which $\langle Z \rangle = 0$, for graphite and silicate grains and various gas temperatures.

Incidentally, the presence of $\langle Q_{\text{abs}} \rangle$ in equation (23) explains the maxima in $\langle U \rangle$ at $a \sim 100 \text{ \AA}$ (see Figure 4), since Q_{abs} peaks for $2\pi a \sim \lambda$, and the photoelectric emission is primarily from radiation with $\lambda \sim 1000 \text{ \AA}$.

4. Photoelectric Recoil Force

4.1. Theory

The photoelectric force on a grain is given by

$$F_{\text{pe}} = \pi a^2 \sum_Z f(Z) \int_{\nu_Z}^{\nu_H} AY Q_{\text{abs}} \frac{cu_\nu}{h\nu} \sqrt{2m_e} \int_{E_1}^{E_2} \sqrt{E_{\text{el}}} f'_E(E_{\text{el}}) S(Z, a, E_{\text{el}}) dE_{\text{el}} d\nu, \quad (24)$$

where the emission asymmetry factor $A(h\nu, a)$ measures the asymmetry in the emission of photoelectrons over the grain surface, $f'_E(E_{\text{el}})dE_{\text{el}}$ gives the fraction of photoelectrons with kinetic energy E_{el} at infinity, $E_1 = \max[0, -(Z + 1/2)e^2/a]$, $E_2 = h\nu - w - (Z + 1/2)e^2/a$, the recoil suppression factor $S(Z, a, E_{\text{el}})$ accounts for electron emission in directions other than the surface normal, and m_e is the electron mass. An electron with kinetic energy E_{el} at infinity has kinetic energy $E_{\text{el}} + (Z + 1/2)e^2/a$ just after emission; upon normalizing we find that

$$f'_E(E_{\text{el}}) = \frac{f_E[E_{\text{el}} + (Z + 1/2)e^2/a]}{y_1(IP, h\nu)}. \quad (25)$$

We follow the simple prescription of Kerker & Wang (1982) for estimating A . The probability of photoemission from any site on the surface is taken to be proportional to the electric intensity $|\mathbf{E}|^2$ just below the surface at that point. Thus,

$$A(h\nu, a) = \frac{-\int_0^\pi \sin \theta \cos \theta |\mathbf{E}(\theta)|^2 d\theta}{\int_0^\pi \sin \theta |\mathbf{E}(\theta)|^2 d\theta}, \quad (26)$$

where θ is the polar angle with respect to the direction of the incident radiation. The electric field $\mathbf{E}(\theta)$ is evaluated using Mie theory (Bohren & Huffman 1983). In Figures 6 and 7 we display the asymmetry factor $A(h\nu, a)$ as a function of incident photon energy for various grain sizes for graphite and silicate composition, respectively.

We assume that the electrons emerge symmetrically with respect to the local surface normal, with a “cosine-law” angular distribution (i.e. the emission rate at angle ψ with respect to the surface normal $\propto \sin \psi \cos \psi$). For an uncharged grain, this would imply $S = 2/3$. When the grain is charged, the electron escapes on a hyperbolic trajectory, so that when it is at infinity its velocity vector makes an angle ψ_∞ with respect to the surface normal which differs from the corresponding angle at the surface, ψ . Taking this into account, we find

$$S = \frac{2}{3}\sqrt{1+b} - \frac{b}{2} + \frac{b^2(1+b/2)}{2(1+b)} \left[\ln \left| 1 + \frac{2}{b} \right| + \frac{1}{2} \ln \left(\frac{1+b/2 - \sqrt{1+b}}{1+b/2 + \sqrt{1+b}} \right) \right] + \frac{b^2}{2\sqrt{1+b}}, \quad (27)$$

$$b \equiv \frac{(Z+1)e^2}{aE_{\text{el}}} \quad , \quad (28)$$

where Ze is the grain charge prior to photoelectron emission. For $-1 \leq b \leq 10^4$, the simpler expression

$$S \approx \frac{1.107}{0.4669 + (b + 1.421)^{0.5043}} \quad (29)$$

is accurate to within 0.6%; we adopt this expression in our computations.

4.2. Computational Results

We will express our results for the photoemissive recoil force as $F_{\text{pe}}/F_{\text{rad}}$, where the force due to radiation pressure is

$$F_{\text{rad}} = \pi a^2 \langle Q_{\text{pr}} \rangle \Delta u_{\text{rad}}; \quad (30)$$

$c\Delta u_{\text{rad}}$ is the net energy flux in the radiation field ($\Delta u_{\text{rad}} = u_{\text{rad}}$ for a unidirectional radiation field, and $\Delta u_{\text{rad}} = 0$ for an isotropic radiation field).

In Figures 8 and 9 we show the force results for graphite and silicate grains, respectively. In the smallest grains, a photoelectron does not necessarily emerge from the surface in the same hemisphere in which it was excited. Thus, we set, somewhat arbitrarily, the minimum grain size for these calculations to $l_e = 10 \text{ \AA}$. We note that for a given value of $G\sqrt{T}/n_e$, the results do not change much as the temperature increases from 100 to 10^3 K , especially for the lower curves corresponding to higher ionization potentials, because the expansion

leading to equation (21) remains accurate. Also, $F_{\text{pe}}/F_{\text{rad}}$ decreases for higher $G\sqrt{T}/n_e$ because the higher ionization potentials quench the photoemission. There is no systematic increase or decrease of $F_{\text{pe}}/F_{\text{rad}}$ over the full range of grain sizes, because the increase in the anisotropy of emitted electrons with grain size roughly compensates for the decrease in photoelectric yield. The sharp minimum near 300 \AA in Figure 8 results from a local plateau in the variation of the anisotropy with grain size, which lies near the maximum of F_{rad} . In Figure 10 we show the effect of varying T_c over a range from 2×10^4 to $5 \times 10^4 \text{ K}$, characteristic of hot stars, using graphite grains and a gas temperature of 100 K as an example.

5. Radiation Anisotropy

In the next section we will estimate the speeds with which grains drift relative to gas, in various interstellar environments. Thus, we first estimate the radiation field anisotropy in the diffuse ISM, by considering the solar neighborhood to be typical and adding up the flux density over the entire sky. Most of the flux in the visible and UV comes directly from stars; also starlight scattered off of dust grains (the diffuse galactic light, DGL) makes a non-negligible contribution (see, e.g., Witt 1989). Ideally, we would like to have a catalog of stars with accurate photometry and complete down to the magnitude beyond which fainter stars do not significantly contribute, along with accurate photometry of the DGL.

Although this ideal is not currently available, there are a few catalogs from which useful estimates can be made. The Skymap Star Catalog, Version 3.7 (Slater & Hashmall 1992) is claimed to be complete down to magnitude 9 in the B and V bands, and the Tycho Catalog (ESA 1997) is claimed to be 99.9% complete down to $V \sim 10.5$. However, the photometry is missing for thousands of stars in the Tycho Catalog, including many bright stars. In Figure 11 we plot the integrated energy densities per unit frequency u_ν , normalized to the ISRF of equation (16), as a function of the limiting stellar magnitude. The Skymap results are for the Johnson B and V bands (B_J and V_J respectively) and the Tycho bands B_T and V_T closely resemble the corresponding Johnson bands. The Tycho catalog also gives indirectly-derived values for V_J for all stars, including those for which Tycho photometry is missing. The B_T and V_T energy densities are systematically lower than the B_J and V_J energy densities due to omission of stars lacking Tycho photometry. The V_J fluxes from the two catalogs agree very well, except at the limit of the Skymap catalog. Note that at magnitude 10 the curves are still concave up, with the integrated starlight accounting for less than half of the ISRF.

The normalized starlight dipole moment is given by

$$\mathbf{p}_s = \frac{\sum_s u_\nu(s) \hat{\mathbf{n}}(s)}{u_\nu(\text{ISRF})}, \quad (31)$$

where $u_\nu(s)$ is the energy density per frequency interval due to star s and $\hat{\mathbf{n}}(s)$ is the direction to star s . In Figure 12 we plot p_s . Again, the B_T and V_T results are offset, because of the absence of photometry for bright stars. The abrupt decrease in the V band normalized dipole moment at the faint end of the Skymap catalog is probably incorrect. It is unlikely that the fainter stars and DGL would conspire to produce an anisotropy directed opposite to that resulting from the brighter stars; thus it appears that the anisotropy in B (V) is at least 5% (3%). For B , the (right ascension, declination) of the anisotropy remain quite constant for limiting magnitudes of 4 through 9, with value $(115^\circ, -43^\circ)$. For V , the anisotropy direction gradually shifts to $(115^\circ, -51^\circ)$ at magnitude 10.5.

The best available catalog for studying the anisotropy in the UV was constructed by the S2/68 experiment (Boksenberg et al. 1973) on the European Space Research Organization’s TD-1 satellite, which provided broadband flux measurements in four channels. The full catalog was not published, but Gondhalekar, Phillips, & Wilson (1980) presented tables of the integrated starlight in hundreds of patches, covering the entire sky. Gondhalekar et al. also estimated the flux contribution from the DGL and from stars too faint to be included in the catalog, using background data. In some cases, two or more stars were observed simultaneously. Such blended stars were excluded from the catalog, and Gondhalekar et al. estimated their contribution to the total flux, although the distribution of these unresolved stars on the sky was not reported. The Mathis et al. (1983) ISRF was constructed to maximize consistency with the Gondhalekar et al. (1980) results and with other, limited-coverage UV surveys. The adopted ISRF fluxes are somewhat higher than the total fluxes of Gondhalekar et al.

In estimating the dipole in the UV, we use tables of integrated starlight in $10^\circ \times 10^\circ$ patches in Gondhalekar (1989). These differ somewhat from the fluxes in Gondhalekar et al. (1980), because the absolute calibration of the S2/68 experiment was revised. In Table 2 we give νu_ν and the normalized dipole moment p_s for the four UV bands; the listed dipole moments are likely lower limits. Note that the normalized dipole moment is substantially greater in the UV than in the visible. This difference presumably results from the differences in the stellar populations giving rise to the two spectral regions and the greater importance of extinction by dust in the UV. The UV radiation is dominated by early-type stars, which are relatively few in number and hence less evenly distributed than main sequence stars in general, all of which contribute to the visible radiation. In Table 3 we display the direction of the anisotropy for all of the considered bands.

For simplicity, we will assume that the anisotropy is independent of wavelength when calculating drift speeds. We will adopt an anisotropy of 10%, intermediate between the anisotropies inferred for the visible and the UV.

6. Drift Speeds

The total force due to the radiation, $F = F_{\text{rad}} + F_{\text{pe}}$, causes the grains to drift with respect to the gas. For the conditions considered here the drag force is approximately proportional to the drift speed (Draine & Salpeter 1979):

$$F_{\text{drag}} \approx \frac{8}{3} n_{\text{H}} v_{\text{d}} a^2 (2\pi m_p kT)^{1/2} (1 + 0.2) (1 + \zeta) \equiv \kappa v_{\text{d}}, \quad (32)$$

where m_p is the proton mass, n_{H} is the H nucleus number density, and $n_{\text{He}}/n_{\text{H}} = 0.1$ is assumed. The factor ζ accounts for the Coulomb drag due to the ions in the gas and is given by

$$\zeta \approx \frac{1}{2(1 + 0.2)} \sum_i x_i \left(\frac{m_i}{m_p} \right)^{1/2} \sum_Z f(Z) \left(\frac{Ze^2}{akT} \right)^2 \ln \left[\frac{3(kT)^{3/2}}{2e^3 |Z| (\pi x n_{\text{H}})^{1/2}} \right], \quad (33)$$

where the sum is over ions i , and $x = \sum_i x_i$. The dominant ion in neutral gas is C^+ , and the abundance of carbon is $\text{C}/\text{H} = 4.0 \times 10^{-4}$ (Grevesse et al. 1991); about half of the C is in the gas phase. Thus, when calculating ζ , we assume $x_{\text{C}} = x$ when $x \leq 2.0 \times 10^{-4}$ and $x_{\text{C}} = 2.0 \times 10^{-4}$, $x_{\text{H}} = x - 2.0 \times 10^{-4}$ when $x > 2.0 \times 10^{-4}$.

In the presence of a magnetic field \mathbf{B} , the steady state drift velocity is given by

$$(v_{\parallel}, v_{\perp}, v_{\perp\perp}) = \frac{F}{\kappa} \left(\cos \theta, \frac{\sin \theta}{1 + (\omega\tau)^2}, \frac{(\omega\tau) \sin \theta}{1 + (\omega\tau)^2} \right) \quad (34)$$

where θ is the angle between \mathbf{B} and \mathbf{F} , $\omega\tau = ZeB/c\kappa$ is the product of the gyrofrequency and gas-drag time, and the subscripts (\parallel , \perp , $\perp\perp$) denote components (parallel to \mathbf{B} , perpendicular to \mathbf{B} and in the plane spanned by \mathbf{B} and \mathbf{F} , perpendicular to the plane spanned by \mathbf{B} and \mathbf{F}).

In Figures 13 and 14 we show v_{d} as a function of a for graphite and silicate grains, respectively, and assuming that \mathbf{F} is parallel to \mathbf{B} . We give results for the cold neutral medium ($n_{\text{H}} = 30 \text{ cm}^{-3}$, $x = 10^{-3}$, ISRF), the warm neutral medium ($n_{\text{H}} = 0.3 \text{ cm}^{-3}$, $x = 0.1$, ISRF), and the combinations ($x = 1.5 \times 10^{-4}$; $T = 100, 10^3 \text{ K}$; $G/n_{\text{H}} = 0.01, 0.1 \text{ cm}^3$; $T_{\text{c}} = 3 \times 10^4 \text{ K}$), which are characteristic of well-known photodissociation regions (PDRs). For the latter combinations, we have adopted $n_{\text{H}} = 10^3 \text{ cm}^{-3}$. These curves remain

accurate to within $\approx 40\%$ for $10 \text{ cm}^{-3} < n_{\text{H}} < 10^5 \text{ cm}^{-3}$. (The slight dependence on n_{H} results from the dependence of the Debye length on n_{H} , in the logarithm in equation 33.) For the diffuse ISM, we assume the anisotropy in the ISRF to be $\Delta u_{\text{rad}} = 0.1$. For most of the cases shown, the Coulomb drag exceeds the drag due to collisions with neutrals despite the low fractional ionization. Since $\zeta \propto T^{-2} \ln T^{3/2}$, v_{d} is generally greater for $T = 1000 \text{ K}$ than for $T = 100 \text{ K}$.

The drift speed does not vary systematically with G/n_{H} or x (e.g. for some sets of values of T and G/n_{H} , v_{d} increases with x while for other sets v_{d} decreases with x), because of the ways in which F_{pe} and ζ depend on these parameters. For a given value of x , ζ increases with G/n_{H} , because of the increased charging, but F_{pe} also increases, since its decrease due to the higher grain charge is more than compensated by the greater radiation intensity. Note that in Figure 13 the curve for $T = 100 \text{ K}$ and $G/n_{\text{H}} = 0.1$ actually lies substantially below the curve for $G/n_{\text{H}} = 0.01$; for the adopted values of T and x , the grain charge is very close to zero when $G/n_{\text{H}} = 0.01$, suppressing the Coulomb drag. For a given value of G/n_{H} , F_{pe} increases with x because the grain charge decreases. The dependence of ζ on x is more complicated; higher values of x and grain charge Z yield higher values of ζ , but Z is lower for higher x .

In Figure 15 we plot $\omega\tau$ for the same conditions as in Figures 13 and 14, and with $Z = \langle |Z| \rangle$. We assume that $B = 5 \mu\text{G}$ in the diffuse ISM and that $B/n_{\text{H}} = 0.01 \mu\text{G cm}^3$ for the PDR-like conditions. As seen in Figure 4, $\langle U \rangle$ remains fairly constant over a wide range of grain sizes, so that, roughly, $\langle |Z| \rangle \propto a$. Also $\kappa \propto a^2$, so that, roughly, $\omega\tau \propto 1/a$.

7. Grain-Grain Collisions and Changes in Dust/Gas Ratio

Since grains of different sizes drift with different speeds, grains collide, with coagulation likely at low collision speeds. As $a \rightarrow 0$, $v_{\text{d}} \rightarrow 0$, so that if grains always stick upon colliding, the timescale t_a for a very small grain to become attached to another grain is given by

$$t_a^{-1} \approx \pi \int_{a_{\text{min}}}^{a_{\text{max}}} a^2 v_{\text{d}}(a) \frac{dn_{\text{gr}}}{da} da. \quad (35)$$

Here we estimate the maximum likely values for t_a in the CNM and WNM. We assume that the radiation field is $\approx 10\%$ anisotropic, and that the anisotropy direction is parallel to the magnetic field. The results are insensitive to the choice of grain size distribution, where we have considered the MRN (Mathis, Rumpl, & Nordsieck 1977) distribution and those derived in Appendix A for environments with $R_V = 3.1$. For coagulation with the graphite population, $t_a \approx 2 \times 10^9 \text{ yr}$ (10^{10} yr) in the CNM (WNM). For coagulation with the silicate population, $t_a \approx 8 \times 10^9 \text{ yr}$ ($3 \times 10^{10} \text{ yr}$) in the CNM (WNM). Thus, drift due to

radiation pressure and the photoelectric force apparently result in negligible coagulation in the diffuse ISM. However, there may be other forces associated with anisotropic radiation, including the recoil force due to photodesorbed adatoms and H_2 molecules which form on the grain surface. We will explore this possibility in a future paper. Also, turbulence can lead to grain-grain collisions (see e.g. Draine 1985).

Gas-grain drift can also lead to variations in the dust-to-gas ratio. If the size of a cold neutral medium region is $\sim 1\text{pc}$, then the time to separate micron-sized grains from the region could be as short as $\approx 10^6\text{yr}$, which is perhaps shorter than the cloud lifetime. When a hot star is located near a molecular cloud, the intense UV radiation can lead to interesting grain dynamics in the resulting photodissociation region (PDR). This will be the subject of a future paper; for a preliminary overview, emphasizing the implications for gas heating in PDRs, see Weingartner & Draine (1999).

8. Photoelectric Heating

8.1. Efficiencies

The photoelectric gas heating rate per grain is given by

$$\Gamma'_{\text{pe}}(a) = \pi a^2 \sum_Z f(Z) \int_{\nu_Z}^{\nu_H} Y Q_{\text{abs}} \frac{cu_\nu}{h\nu} \int_{E_1}^{E_2} E_{\text{el}} f'_E(E_{\text{el}}) dE_{\text{el}} d\nu, \quad (36)$$

where $f'_E(E_{\text{el}})$ is defined in equation (25). We compute the total efficiency for conversion of absorbed radiation into gas heating,

$$\epsilon_\Gamma(a) = \frac{\Gamma'_{\text{pe}}(a) - \Lambda'(a)}{\pi a^2 cu_{\text{rad}} \langle Q_{\text{abs}} \rangle} \quad (37)$$

Here $\Lambda'(a)$ is the rate of energy removal from the gas due to the accretion of charged particles onto the grain, and is given by

$$\Lambda'(a) = \sum_i n_i s_i \left(\frac{8kT}{\pi m_i} \right)^{1/2} \pi a^2 \tilde{\Lambda}(\eta_i, \xi_i) kT, \quad (38)$$

where the sum runs over electrons and ions and η_i and ξ_i are defined below equation (14). Expressions for $\tilde{\Lambda}$ can be found in Draine & Sutin (1987).

Figures 16 through 18 show results for the gas heating efficiency for the same conditions as noted for the force computations displayed in Figures 8 through 10. The heating efficiency generally decreases for increasing $G\sqrt{T}/n_e$. The discontinuity at $a = 5\text{\AA}$ in the curve for the WNM in Figure 16 is due to a change in Z_{EA} from 1 for smaller grains to 2 for larger ones.

8.2. Net Photoelectric Heating Rate

In Figure 19 we display some of the candidate grain size distributions obtained in Appendix A, and in Figure 20 we plot the net total gas heating per H nucleus and per Habing flux,

$$\frac{\Gamma_{\text{tot}}}{Gn_{\text{H}}} = \sum_{g,s} \int_{a_{\text{min}}}^{a_{\text{max}}} \frac{\Gamma'_{\text{pe}} - \Lambda'}{G} \frac{1}{n_{\text{H}}} \frac{dn_{\text{gr}}}{da} da \quad (39)$$

as a function of $G\sqrt{T}/n_e$ for these distributions, with $T = 100$ K and $T_c = 3 \times 10^4$ K. The sum is over the graphite and silicate populations. The heating rates obtained for the several distributions span about an order of magnitude, showing the importance of the grain size distribution.

For comparison, we also plot the Bakes & Tielens (1994) result in Figure 20. The Bakes & Tielens result lies between our results for the $R_V = 3.1$ distributions with $f_g = 0$ and 0.1.

The photoelectric heating rate for the grain distributions of Appendix A is fairly well reproduced by the following function:

$$\Gamma_{\text{pe}} \equiv \sum_{g,s} \int_{a_{\text{min}}}^{a_{\text{max}}} \Gamma'_{\text{pe}}(a) \frac{dn_{\text{gr}}}{da} da = 10^{-26} \frac{\text{erg}}{\text{s}} Gn_{\text{H}} \frac{C_0 + C_1 T^{C_4}}{1 + C_2 (G\sqrt{T}/n_e)^{C_5} [1 + C_3 (G\sqrt{T}/n_e)^{C_6}]}, \quad (40)$$

where T is in K and $G\sqrt{T}/n_e$ is in $\text{K}^{1/2} \text{cm}^3$. Values for the seven parameters in equation (40) are given in Table 4, as well as the largest fractional error, err , for $10 \leq T \leq 10^4$ K and $10^2 \leq G\sqrt{T}/n_e \leq 10^6 \text{K}^{1/2} \text{cm}^3$. In general, we consider a blackbody spectrum with $T_c = 3 \times 10^4$ K; we also consider the ISRF for $R_V = 3.1$.

Bakes & Tielens (1994) neglect heating from grains with $a > 100$ Å. This is a good approximation for the highest values of $G\sqrt{T}/n_e$, but we find that the heating from larger grains can contribute significantly for low $G\sqrt{T}/n_e$. This is demonstrated in Table 4, where we give the fraction h_s of the total heating due to grains with $a < 100$ Å, for $G\sqrt{T}/n_e = 10^2 \text{K}^{1/2} \text{cm}^3$ and $T = 100$ K. For $R_V = 4.0$, $f_g = 0.03$, and $T_c = 3 \times 10^4$ K, e.g., 36% of the heating is contributed by grains with $a > 100$ Å. Bakes & Tielens also neglect the heating contributed by silicate grains. We find that silicates contribute less than 10% as much heating as graphite when $G\sqrt{T}/n_e \sim 10^6 \text{K}^{1/2} \text{cm}^3$. However, the silicate contribution increases as $G\sqrt{T}/n_e$ decreases, and is comparable to or exceeds the graphite contribution when $G\sqrt{T}/n_e \sim 10^2 \text{K}^{1/2} \text{cm}^3$.

The rate of cooling due to charged particle accretion is significant, compared with the photoelectric heating rate, when $T \gtrsim 10^3$ K. The following approximation is fairly accurate

when $10^3 \leq T \leq 10^4$ K and $10^2 \leq G\sqrt{T}/n_e \leq 10^6$ K^{1/2} cm³:

$$\Lambda = 10^{-28} \frac{\text{erg}}{\text{s}} G n_{\text{H}} \exp \left\{ D_0 - D_1 \left[\ln \left(\frac{G\sqrt{T}}{n_e} \right) - D_2 \right]^2 + \left[D_3 + D_4 \left(\frac{G\sqrt{T}}{n_e} \right)^{-D_5} \right] \ln T \right\}. \quad (41)$$

Here T is in K, $G\sqrt{T}/n_e$ is in K^{1/2} cm³, and the values of the six parameters are given in Table 5.

8.3. Heating and Cooling in H II Regions

In H II regions, the radiation field includes photons with $h\nu > 13.6$ eV. To see the possible importance of these photons, we calculate integrated photoelectric heating and recombination cooling rates for blackbody spectra with no upper cutoff energy, adopting $T_c = 3.5 \times 10^4$ and 4.5×10^4 K. Of course, at any given location in an H II region, there will be a break in the spectrum at 13.6 eV, due in part to absorptions along the path to the star and in part to the break in the stellar spectrum itself. Thus, spectra with no break and with a cutoff at 13.6 eV should roughly bracket the range applicable in H II regions.

We take $n_e/n_{\text{H}} = 1$ and $T = 9000$ K for the gas. In Tables 6 and 7, we give $\Gamma_{\text{pe}}/Gn_{\text{H}}$ and Λ/Gn_{H} for $G/n_{\text{H}} = 0.1, 1$, and 10 cm³, both with and without the cutoff at 13.6 eV, for several of the grain size distributions obtained in Appendix A. The heating rate is affected by as much as an order of magnitude and the cooling rate is modestly affected, due to changes in the charging. When $G/n_{\text{H}} < 0.1$ cm³ the grains are negatively charged, so that there is little change in $\Gamma_{\text{pe}}/Gn_{\text{H}}$ with G/n_{H} , and $\Lambda/Gn_{\text{H}} \propto (G/n_{\text{H}})^{-1}$, roughly.

9. Summary

1. We estimate the photoemissive recoil force on graphite and silicate grains, finding that it can exceed the direct radiation force and should therefore be included in studies of dust dynamics when radiation pressure is important (see Figures 8 and 9).
2. Using nearly complete star catalogs, we estimate that the starlight radiation field in the solar neighborhood is $\sim 10\%$ anisotropic in the visible and UV (§5).
3. We estimate grain drift speeds in the diffuse ISM and in photodissociation regions, and find values as high as ~ 1 km s^{−1} for large silicate grains in the warm neutral medium (see Figures 13 and 14).
4. We compute the efficiency with which grains convert absorbed radiation into gas

heating, as a function of grain size (§8.1, Figures 16 – 18).

5. We obtain size distributions for graphite-silicate mixtures which reproduce the wavelength-dependent extinction for $R_V = 3.1, 4.0,$ and 5.5 , with various populations of ultrasmall carbonaceous grains (Figure 19 and Appendix A).

6. We integrate the net gas heating rate over these grain size distributions (Figure 20), and we provide fitting functions for the resulting total photoelectric heating and recombination cooling rates (§8.2). We also tabulate heating and cooling rates for conditions typical of H II regions (Tables 6 and 7).

7. The details of photoelectric emission from interstellar grains remain uncertain, due both to uncertainties in the physics of photoelectric emission from small particles and to our limited progress in determining the composition and geometry of interstellar dust. The results presented here represent our best estimates for small silicate and carbonaceous particles.

8. We have investigated a range of grain sizes, gas temperatures, radiation field color temperatures, and ratios G/n_e of radiation intensity to electron density, and selected results have been presented. Interested readers can acquire computational results in electronic form, as well as a FORTRAN routine that implements the heating and cooling approximations of equations (40) and (41), on the World Wide Web at www.astro.princeton.edu/~josephw/index.html.

This research was supported in part by NSF grant AST-9619429 and by an NSF Graduate Research Fellowship to JCW. We are grateful to R. H. Lupton for the availability of the SM plotting package.

A. Appendix: Grain Size Distributions

The MRN grain size distribution was derived to reproduce the observed extinction through the diffuse ISM using bare graphite and silicate grains (Mathis, Rumpl, & Nordsieck 1977); the expression for the grain number density in this model is

$$dn_{\text{gr}} = C n_{\text{H}} a^{-3.5} da, \quad a_{\text{min}} < a < a_{\text{max}} \quad (\text{A1})$$

with $C = 10^{-25.13}$ ($10^{-25.11}$) $\text{cm}^{3.5}$ for graphite (silicate) grains (Draine & Lee 1984), $a_{\text{min}} = 50 \text{ \AA}$, and $a_{\text{max}} = 0.25 \mu\text{m}$.

Since the development of the MRN model, more observational constraints have become available. Observations of 3 to $60 \mu\text{m}$ infrared emission, presumably generated by grains

small enough to reach temperatures of 30 to 300 K or more upon the absorption of a single starlight photon (see e.g. Draine & Anderson 1985), imply a population of very small grains (with $a < 50 \text{ \AA}$). The non-detection of the $10\mu\text{m}$ silicate feature in emission from diffuse clouds (Mattila et al. 1996; Onaka et al. 1996) appears to rule out silicate grains with $a \lesssim 15 \text{ \AA}$. Graphite grains with $a \lesssim 3.5 \text{ \AA}$ are expected to be unstable against sublimation in the interstellar radiation field (Guhathakurta & Draine 1989). Recent observations of dust-correlated microwave emission has been attributed to the very small grain population (Draine & Lazarian 1998a).

The abundance of very small grains required to generate the observed IR emission from the diffuse ISM is not yet well-known. In the model of Désert, Boulanger, & Puget (1990), 9% of the cosmic C is in polycyclic aromatic hydrocarbon (PAH) molecules with less than 540 C atoms (equal to the number of C atoms in a spherical graphite grain with $a \approx 11 \text{ \AA}$). Draine & Lazarian (1998b) estimated the electric dipole radiation from spinning grains. They considered an MRN distribution with a_{min} extended down to 3.5 \AA for graphite plus an additional population of very small carbonaceous grains with a log-normal size distribution:

$$\frac{1}{n_{\text{H}}} \frac{dn_{\text{gr}}}{da} = D(a) \equiv Ba^{-1} \exp \left\{ -\frac{1}{2} \left[\frac{\ln(a/a_0)}{\sigma} \right]^2 \right\}, \quad a > 3.5 \text{ \AA} \quad (\text{A2})$$

$$B = \frac{7.64 \times 10^{-28} \text{ cm}^3 f_g \exp(-4.5\sigma^2)}{a_0^3 \sigma \left\{ 1 + \text{erf}[3\sigma/\sqrt{2} + \ln(a_0/3.5 \text{ \AA})/\sigma\sqrt{2}] \right\}}, \quad (\text{A3})$$

where f_g is the fraction of the cosmic C in the log-normal population. Draine & Lazarian adopted $a_0 = 3 \text{ \AA}$ and $\sigma = 0.5$ and found that the dipole radiation could account for the dust-correlated component of the diffuse Galactic microwave emission if $f_g \approx 0.05$.

Our goal here is to find an overall grain size distribution which includes very small carbonaceous grains and is consistent with the observed extinction. For simplicity, we assume that the grains consist of bare graphite and silicate spheres, with dielectric functions as given by Draine & Lee (1984)³ and Laor & Draine (1993). We adopt the following form

³The “astronomical silicate” dielectric function $\epsilon = \epsilon_1 + i\epsilon_2$ of Draine & Lee (1984), based on laboratory measurements of crystalline olivine in the ultraviolet (Huffman & Stapp 1973), contains a feature at $6.5\mu\text{m}^{-1}$. Kim & Martin (1995) have pointed out that this feature, which is of crystalline origin, is not present in the observed interstellar extinction or polarization. We have therefore excised this feature from ϵ_2 , and recomputed ϵ_1 using the Kramers-Kronig relation (Draine & Lee 1984). The resulting “smoothed astronomical silicate” dielectric functions are available on the World Wide Web at www.astro.princeton.edu/~draine/index.html

for the distribution:

$$\frac{1}{n_{\text{H}}} \frac{dn_{\text{gr}}}{da} = D(a) + \frac{C_{\text{g}}}{a} \times \begin{cases} (a/a_{\text{t,g}})^{\alpha_{\text{g}}}, & 3.5 \text{ \AA} < a < a_{\text{t,g}} \\ (a/a_{\text{t,g}})^{\beta_{\text{g}}} \exp[(a_{\text{t,g}}/a_{\text{c,g}})^3 - (a/a_{\text{c,g}})^3], & a_{\text{t,g}} < a < a_{\text{max,g}} \end{cases} \quad (\text{A4})$$

for graphite and

$$\frac{1}{n_{\text{H}}} \frac{dn_{\text{gr}}}{da} = \frac{C_{\text{s}}}{a} \times \begin{cases} (a/a_{\text{t,s}})^{\alpha_{\text{s}}}, & a_{\text{min,s}} < a < a_{\text{t,s}} \\ (a/a_{\text{t,s}})^{\beta_{\text{s}}} \exp[(a_{\text{t,s}}/a_{\text{c,s}})^3 - (a/a_{\text{c,s}})^3], & a_{\text{t,s}} < a < a_{\text{max,s}} \end{cases} \quad (\text{A5})$$

for silicate. We adopt the same values for a_0 and σ as Draine & Lazarian (1998b)⁴. For a given value of f_{g} , we seek the best fit to the extinction by varying the powers α_{g} , β_{g} , α_{s} , and β_{s} ; the transition sizes $a_{\text{t,g}}$ and $a_{\text{t,s}}$; the lower cutoff size $a_{\text{min,s}}$; the upper cutoff parameters $a_{\text{c,g}}$ and $a_{\text{c,s}}$; and the total volume per H in both the graphite and silicate distributions.

The extinction at wavelength λ is given by

$$A(\lambda) = (2.5\pi \log e) \int d \ln a \frac{dN_{\text{gr}}(a)}{da} a^3 Q_{\text{ext}}(a, \lambda), \quad (\text{A6})$$

where $N_{\text{gr}}(a)$ is the column density of grains with size $\leq a$ and Q_{ext} is the extinction efficiency factor, evaluated using Mie theory. The extinction curve (i.e. the functional dependence of the extinction on the wavelength) varies depending upon the interstellar environment through which the starlight passes. Cardelli, Clayton, & Mathis (1989, CCM) found that this dependence can be fairly well-characterized by a single parameter, which they took to be $R_V \equiv A(V)/E(B - V)$, the ratio of total to selective extinction. CCM have fitted the average extinction curve $A(\lambda)/A(V)$ as functions of λ and R_V . For the diffuse ISM, $R_V \approx 3.1$; higher values are observed for dense clouds. Bohlin, Savage, & Drake (1978) found that the ratio of the total neutral hydrogen column density N_{H} (including both atomic and molecular forms) to $E(B - V)$ is fairly constant for the diffuse ISM, with value $5.8 \times 10^{21} \text{ cm}^{-2}$. This provides the normalization for the extinction curve: $A(V)/N_{\text{H}} = 5.3 \times 10^{-22} \text{ cm}^2$. The normalization is less clear for dense clouds, because of the difficulty in measuring N_{H} . CCM found that $A(\lambda)/A(I)$ appears to be independent of R_V for $\lambda > 0.9 \mu\text{m}$ ($= I$ band) suggesting that the diffuse cloud value of $A(I)/N_{\text{H}} = 2.6 \times 10^{-22} \text{ cm}^2$ may also hold for dense clouds (see, e.g., Draine 1989); we adopt this normalization.

We use the Levenberg-Marquardt method, as implemented in Press et al. (1992), to fit the continuous extinction between $0.3 \mu\text{m}^{-1}$ and $10 \mu\text{m}^{-1}$, and demand that $a_{\text{min}}^{\text{s}} \geq 15 \text{ \AA}$. We evaluate the extinction at 100 points, equally spaced in $\ln \lambda^{-1}$, and minimize the error

⁴Since the grains in the log-normal population all have $a \ll \lambda$, the values of a_0 and σ do not affect the extinction; all that matters is the value of f_{g} .

function $\chi_1^2 = \sum_i (\ln A_{\text{obs}} - \ln A_{\text{mod}})^2 / \sigma_i^2$, where A_{obs} is the average “observed” extinction as given by CCM for a given value of R_V , A_{mod} is the extinction computed for the model (equation A6), and the σ_i are weights. When evaluating A_{mod} , we verify that the integral in equation A6 is evaluated accurately.

For A_{obs} , we adopt the CCM parametrization for $3.3\mu\text{m}^{-1} < \lambda^{-1} < 10\mu\text{m}^{-1}$. For $1.1\mu\text{m}^{-1} < \lambda^{-1} < 3.3\mu\text{m}^{-1}$, we employ the extinction properties from O’Donnell (1994), slightly modified to join smoothly with CCM at $1.1\mu\text{m}^{-1}$ and $3.3\mu\text{m}^{-1}$. The CCM expression for $\lambda^{-1} < 1.1\mu\text{m}^{-1}$ was derived by fitting the data of Rieke & Lebofsky (1985) with a power law; the resulting power law index is 1.61. Draine (1989) considered a different data set and suggested an index of 1.75. Recently, Kenyon, Lada, & Barsony (1998) have derived an index of $1.72^{+0.07}_{-0.06}$ for the ρ Oph dark cloud. Thus, for $\lambda^{-1} < 1.1\mu\text{m}^{-1}$ we employ a power law with index 1.72 normalized to the CCM value at $\lambda^{-1} = 1.1\mu\text{m}^{-1}$. We take the weights $\sigma_i^{-1} = 1$ for $1.1\mu\text{m}^{-1} < \lambda^{-1} < 8\mu\text{m}^{-1}$ and $\sigma_i^{-1} = 1/3$ for $\lambda^{-1} < 1.1\mu\text{m}^{-1}$ and $\lambda^{-1} > 8\mu\text{m}^{-1}$, since the actual IR extinction is uncertain and the CCM expression for $\lambda^{-1} > 8\mu\text{m}^{-1}$ is based on a small number of sight lines.

In Table 8 we list the values of the distribution parameters for which the extinction with $R_V = 3.1, 4.0$, and 5.5 is best fit, for various values of f_g . We report \tilde{V}_g and \tilde{V}_s , the total grain volumes in the graphite (including the log-normal contribution) and silicate populations, normalized to their values in the MRN distribution ($2.67 \times 10^{-27} \text{ cm}^3/\text{H}$ and $2.79 \times 10^{-27} \text{ cm}^3/\text{H}$, respectively). The MRN volumes are close to the maximum possible values given cosmic abundance constraints; our derived volumes exceed the MRN values by as much as $\approx 20\%$. We expect that a model which includes non-spherical grains would produce more extinction per unit grain volume, so we regard our modest violation of cosmic abundance constraints as an artifact due to our use of only spherical grains. We also expect that the total grain volume should not vary substantially from one interstellar environment to another. The lower values for \tilde{V}_g and \tilde{V}_s in the fits for $R_V = 4.0$ and 5.5 probably indicate that a significant fraction of the grain mass is locked up in very large grains which have low extinction efficiencies for the range of wavelengths considered.

We also display χ_1^2 and $\chi_2^2 = \sum_i (\ln A_{\text{obs}} - \ln A_{\text{mod}})^2$. Usually the fit is best for $f_g = 0$, but hardly suffers as long as f_g is not too large. In Figure 21 we display A_{obs} and A_{mod} for $f_g = 0.0$ and the three values of R_V in a log-log plot, to give a sense for the fit quality over the entire range of λ^{-1} . In Figures 22, 23, and 24, we display extinction curves for $f_g = 0$ and for the highest value of f_g included in Table 8; we show the contribution from each of the grain distribution components.

In assessing the quality of these fits, one must bear in mind that (1) the dielectric functions used are certainly not correct in detail, (2) the size distributions are not actually

power laws, and (3) the interstellar grains are appreciably non-spherical. Therefore, a precise fit is not to be expected. Clearly, extinction data do not well constrain f_g . Of course, an ideal grain model would employ all of the observational constraints, including IR emission, and a proper treatment of the extinction efficiency for the very small carbonaceous grains, including PAHs.

REFERENCES

- Bakes, E. L. O., & Tielens, A. G. G. M. 1994, *ApJ*, 427, 822
- Bohlin, R. C., Savage, B. D., & Drake, J. F. 1978, *ApJ*, 224, 132
- Bohren, C. F. & Huffman, D. R. 1983, *Absorption and Scattering of Light by Small Particles* (New York: Wiley)
- Boksenberg, A., Evans, R. G., Fowler, R. G., Gardner, I. S. K., Houziaux, L., Humphries, C. M., Jamar, C., Macau, D., Malaise, D., Monfils, A., Nandy, K., Thompson, G. I., Wilson, R., & Wroe, H. 1973, *MNRAS*, 163, 291
- Burtscher, H. & Schmidt-Ott, A. 1982, *Phys. Rev. Lett.*, 48, 1374
- Burtscher, H., Schmidt-Ott, A., & Siegmann, H.C. 1984, *Z. Phys. B*, 56, 197
- Cardelli, J. A., Clayton, G. C., & Mathis, J. S. 1989 (CCM), *ApJ*, 345, 245
- de Jong, T. 1977, *A&A*, 55, 137
- Désert, Boulanger, & Puget 1990, *A&A*, 237, 215
- Draine, B. T. 1978, *ApJS*, 36, 595
- Draine, B. T. 1985, in *Protostars and Planets II*, ed. D. C. Black & M. S. Matthews (Tucson: Univ. Arizona Press), 621
- Draine, B. T. 1989, in *Infrared Spectroscopy in Astronomy*, ed. B. H. Kaldeich (Paris: ESA)
- Draine, B. T. & Anderson, N. 1985, *ApJ*, 292, 494
- Draine, B. T. & Lazarian, A. 1998a, *ApJ*, 494, L19
- Draine, B. T. & Lazarian, A. 1998b, *ApJ*, 508, 157
- Draine, B. T. & Lee, H. M. 1984, *ApJ*, 285, 89

- Draine, B. T. & Salpeter, E. E. 1979, *ApJ*, 231, 77
- Draine, B. T., & Sutin, B. 1987, *ApJ*, 320, 803
- ESA, 1997, *The Hipparcos and Tycho Catalogues*, ESA SP-1200
- Faraci, G., Pennisi, A. R., & Margaritondo, G. 1989, *Phys. Rev. B*, 40, 4209
- Feuerbacher, B., Anderegg, M., Fitton, B., Laude, L. D., Willis, R. F., & Grard, R. J. L. 1972, *Geochim. Cosmochim. Acta Suppl.* 2,
- Feuerbacher, B. & Fitton, B. 1972, *J. Appl. Phys.*, 43, 1563 3, 2655
- Fujihira, M., Hirooka, R., & Inokuchi, H. 1973, *Chem. Phys. Lett.*, 19, 584
- Gondhalekar, P. M. 1989, in *The Galactic and Extragalactic Background Radiation*, ed. S. Bowyer & C. Leinert (Dordrecht: Kluwer), 49
- Gondhalekar, P. M., Phillips, A. P., & Wilson, R. 1980, *A&A*, 85, 272
- Grevesse, N., Lambert, D. L., Sauval, A. J., van Dishoeck, E. F., Farmer, C. B., & Norton, R. H. 1991, *A&A*, 242, 488
- Guhathakurta, P. & Draine, B. T. 1989, *ApJ*, 345, 230
- Habing, H. J. 1968, *Bull. Astron. Inst. Netherlands*, 19, 421
- Huffman, D. R. & Stapp, J. L. 1973, in *IAU Symposium 52, Interstellar Dust and Related Topics*, ed. J. M. Greenberg & H. C. van de Hulst (Dordrecht: Reidel), 297
- Kenyon, S. J., Lada, E. A., & Barsony, M. 1998, *AJ*, 115, 252
- Kerker, M. & Wang, D.-S. 1982, *J. Coll. Interface Sci.*, 85, 302
- Kim, S.-H. & Martin, P. G. 1995, *ApJ*, 442, 172
- Lafon, J.-P. J. 1990, *A&A*, 235, 490
- Laor, A. & Draine, B. T. 1993, *ApJ*, 402, 441
- Martin, C., Arakawa, E. T., Callcott, T. A., & Warmack, R. J. 1987, *J. Electr. Spectrosc. Rel. Phenom.*, 42, 171
- Mathis, J.S., Mezger, P.G., & Panagia, N. 1983, *A&A*, 128, 212
- Mathis, J. S., Rumpl, W., & Nordsieck, K. H. 1977, *ApJ*, 217, 425

- Mattila, K., Lemke, D., Haikala, L. K., Laureijs, R. J., Léger, A., Lehtinen, K., Leinert, Ch., & Mezger, P. G. 1996, A&A, 315, L353
- McFeely, F. R., Cartier, E., Yarmoff, J. A., & Joyce, S. A. 1990, Phys. Rev. B, 42, 5191
- Mezger, P.G., Mathis, J.S., & Panagia, N. 1982, A&A, 105, 372
- Müller, U., Schmidt-Ott, A., & Burtscher, H. 1988, Z. Phys. B, 73, 103
- Nagaev, E. L. 1992, Phys. Rep., 222, 199
- O'Donnell, J. E. 1994, ApJ, 422, 158
- Onaka, T., Yamamura, I., Tanabé, T., Roellig, T. L., & Yuen, L. 1996, PASJ, 48, L59
- Press, W. H., Teukolsky, S. A., Vetterling, W. T., & Flannery, B. P. 1992, Numerical Recipes in FORTRAN: The Art of Scientific Computing, Second Edition (Cambridge: Cambridge University Press)
- Rieke, G. H. & Lebofsky, M. J. 1985, ApJ, 288, 618
- Schmidt-Ott, A., Schurtenberger, P., & Siegmann, H. C. 1980, Phys. Rev. Lett., 45, 1284
- Slater M. & Hashmall J. 1992, NASA/Goddard Space Flight Center Document 554-FDD-89/001R3UD1
- Tielens, A. G. G. M., & Hollenbach, D. J. 1985, ApJ, 291, 722
- Verstraete, L., Léger, A., d'Hendecourt, L., Dutuit, O., & Défourneau, D. 1990, A&A, 237, 436
- Watson, W. D. 1972, ApJ, 176, 103
- Watson, W. D. 1973, J. Opt. Soc. Am., 63, 164
- Weingartner, J. C. & Draine, B. T. 1999, to appear in The Universe as Seen by ISO, ed. P. Cox & M. F. Kessler
- Witt, A. N. 1989, in The Galactic and Extragalactic Background Radiation, ed. S. Bowyer & C. Leinert (Dordrecht: Kluwer), 127

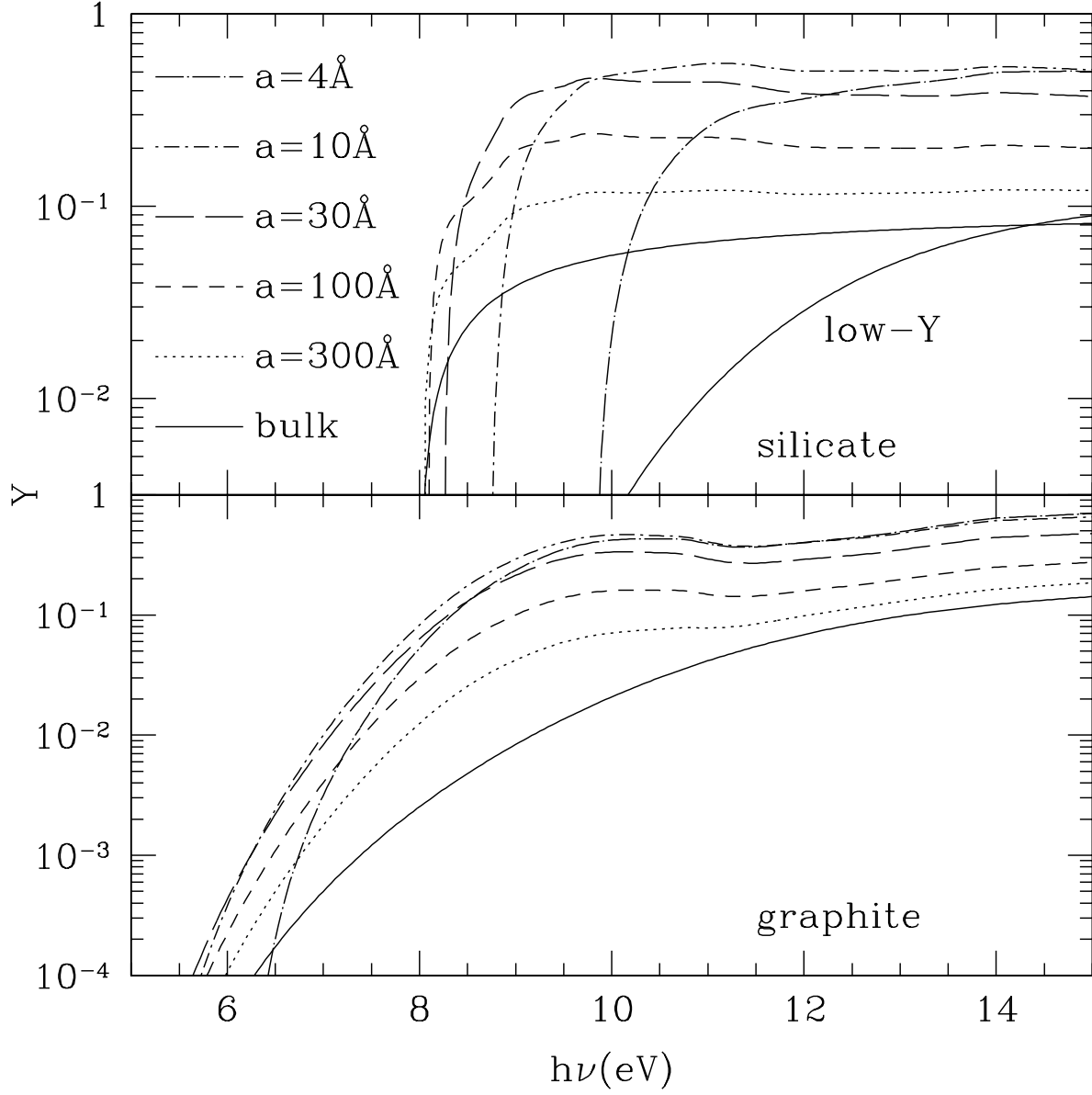


Fig. 1.— Photoelectric yield Y for neutral graphite and silicate grains as a function of incident photon energy $h\nu$, for several values of the grain size a , as indicated. The curve labelled “low-Y” is a low-yield alternative to our adopted silicate yield.

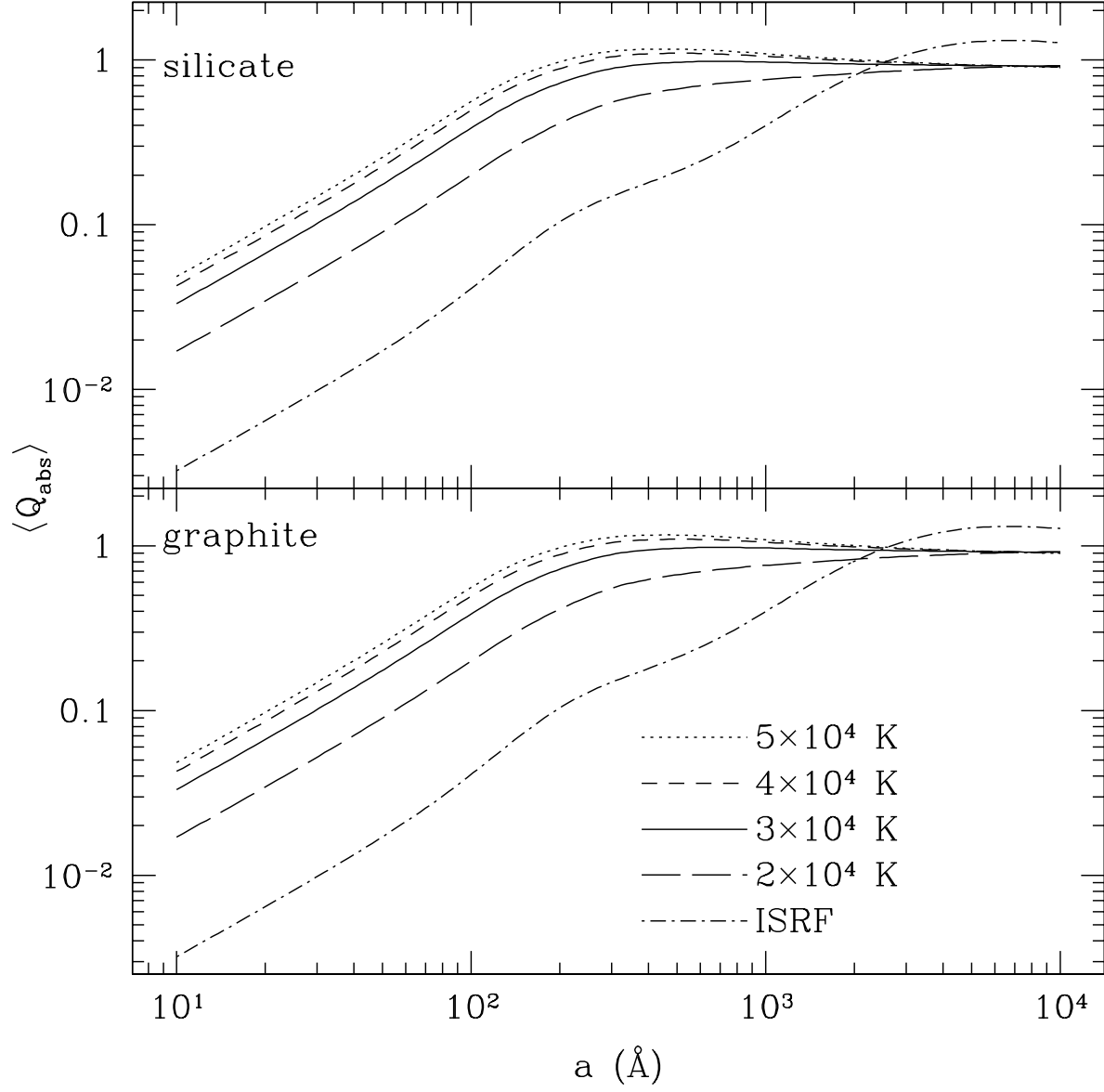


Fig. 2.— Absorption efficiency factors for graphite and silicate grains, averaged over the interstellar radiation field (ISRF) and blackbody spectra with indicated color temperatures.

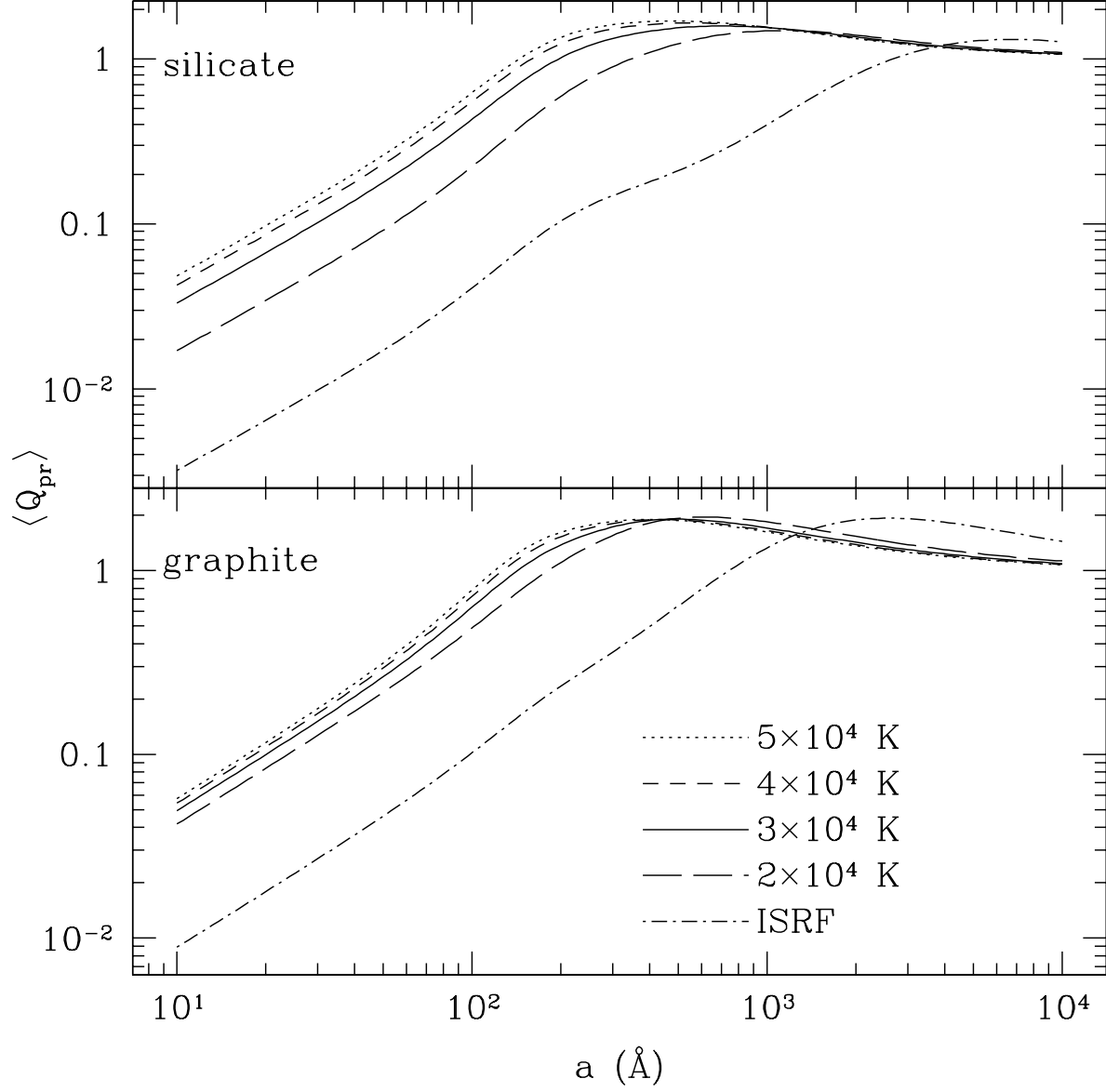


Fig. 3.— Radiation pressure efficiency factors for graphite and silicate grains, averaged over the interstellar radiation field (ISRF) and blackbody spectra with indicated color temperatures.

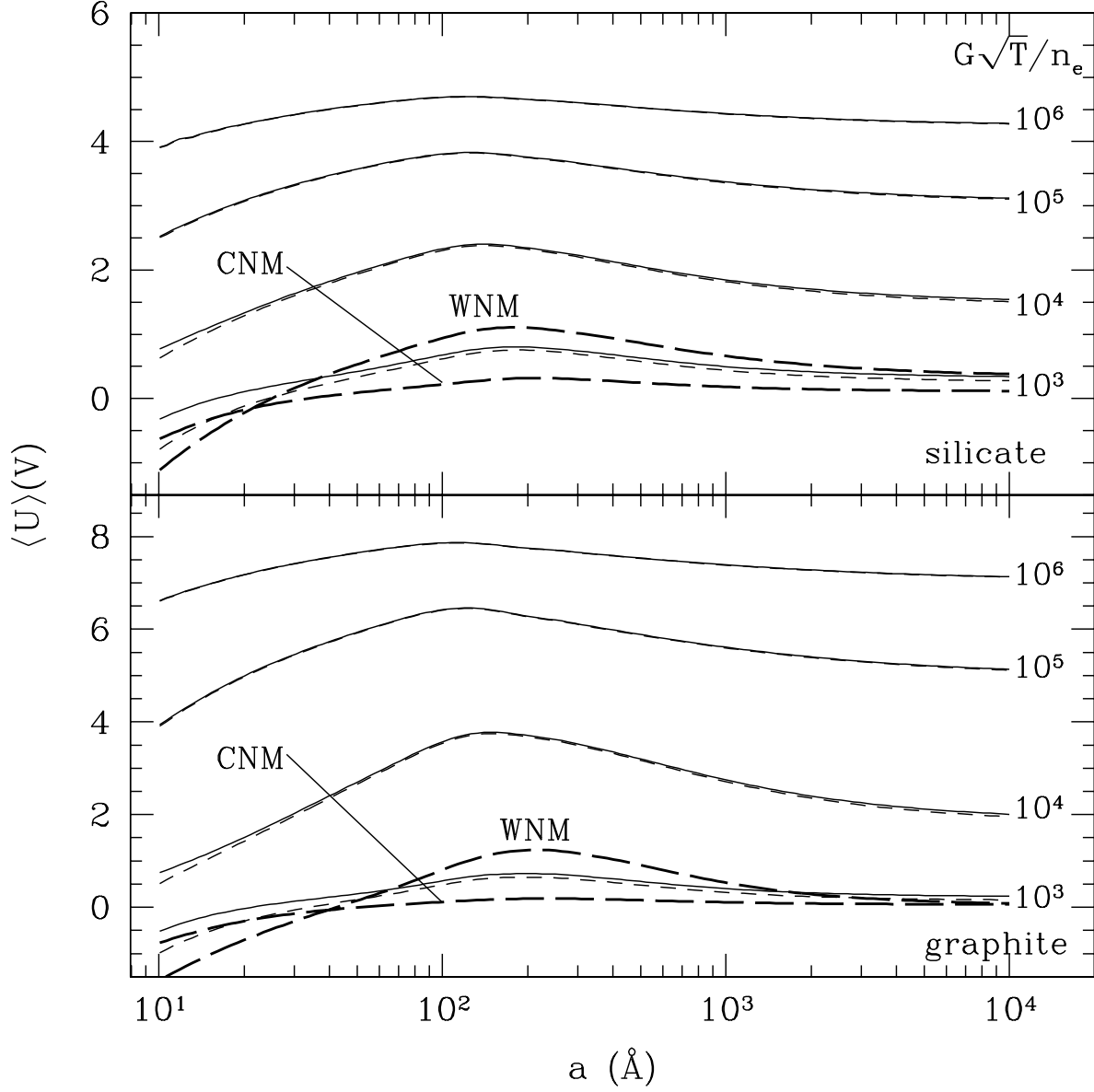


Fig. 4.— Average electrostatic potential $\langle U \rangle$ for $T_c = 3 \times 10^4$ K. The top (bottom) panel is for silicate (graphite) grains; curves labelled CNM (WNM) are for cold (warm) neutral media; solid (short-dashed) lines indicate $T = 100$ K (1000 K). For the $T = 100$ K and 1000 K curves, values of $G\sqrt{T}/n_e$ are indicated in $\text{K}^{1/2} \text{cm}^3$.

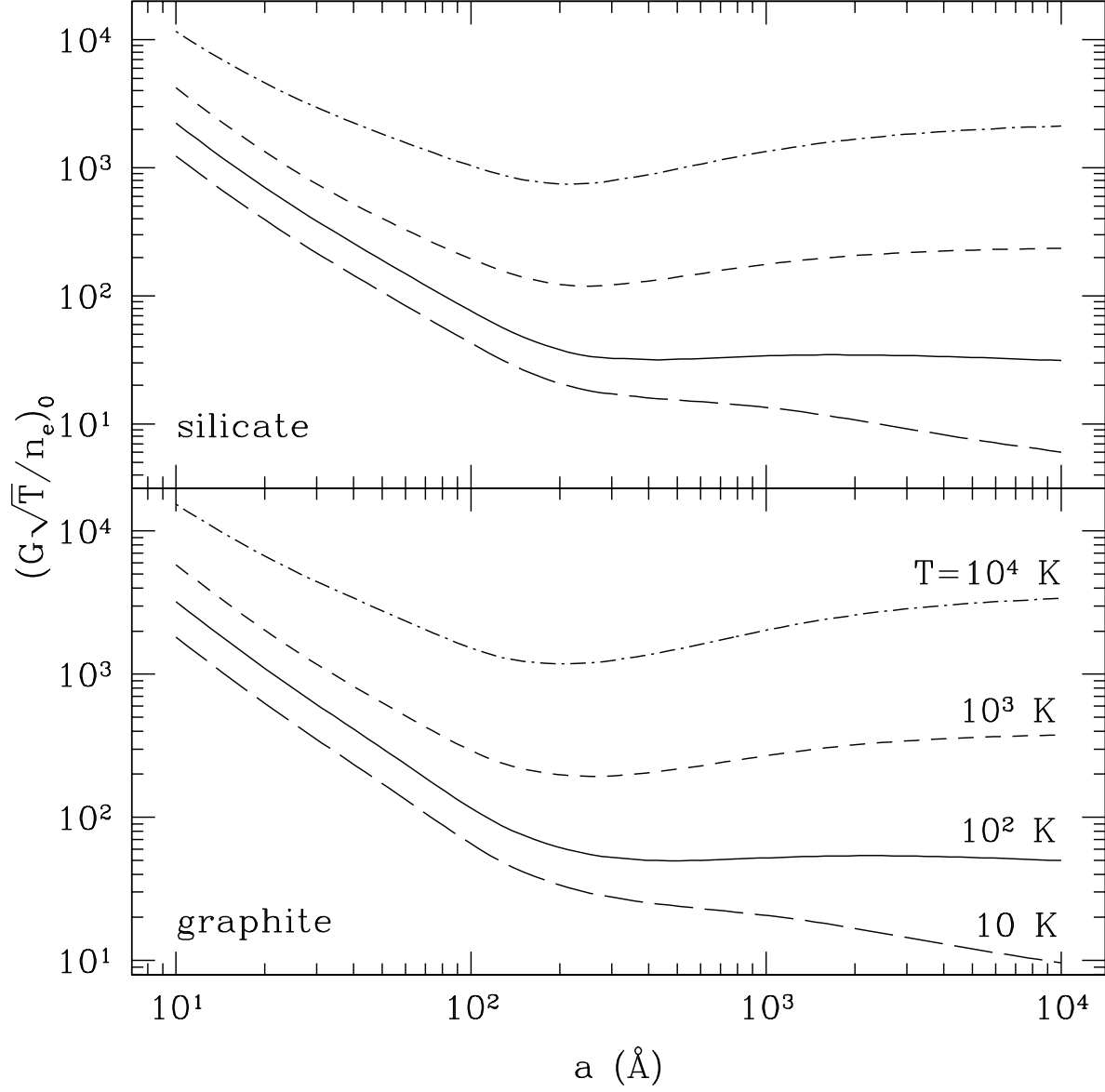


Fig. 5.— The value of the charging parameter for which $\langle Z \rangle = 0$, for graphite and silicate grains and various gas temperatures, as labelled.

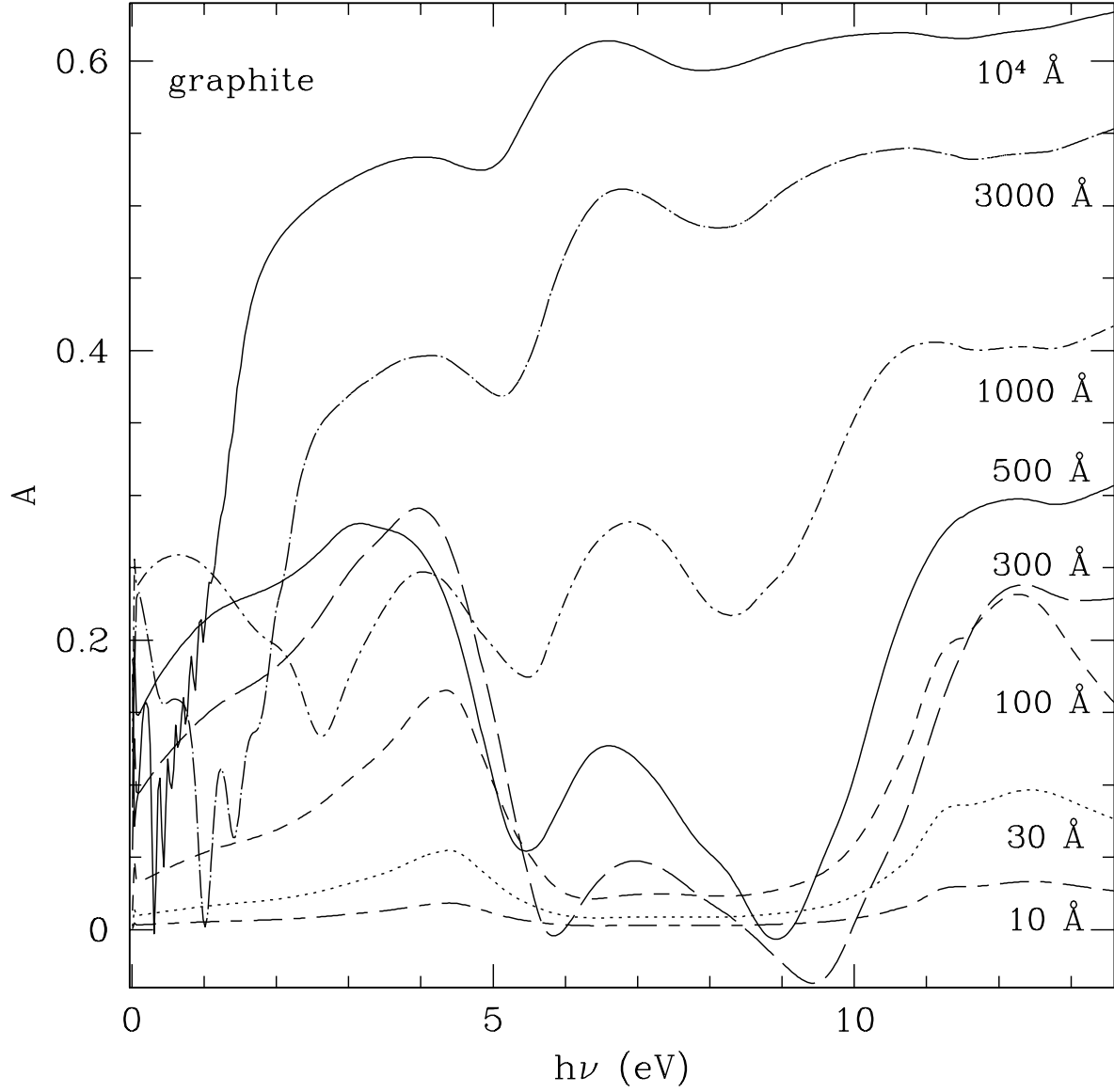


Fig. 6.— The asymmetry factor A as a function of the incident photon energy $h\nu$, for graphite grains. The grain radius is indicated for each curve.

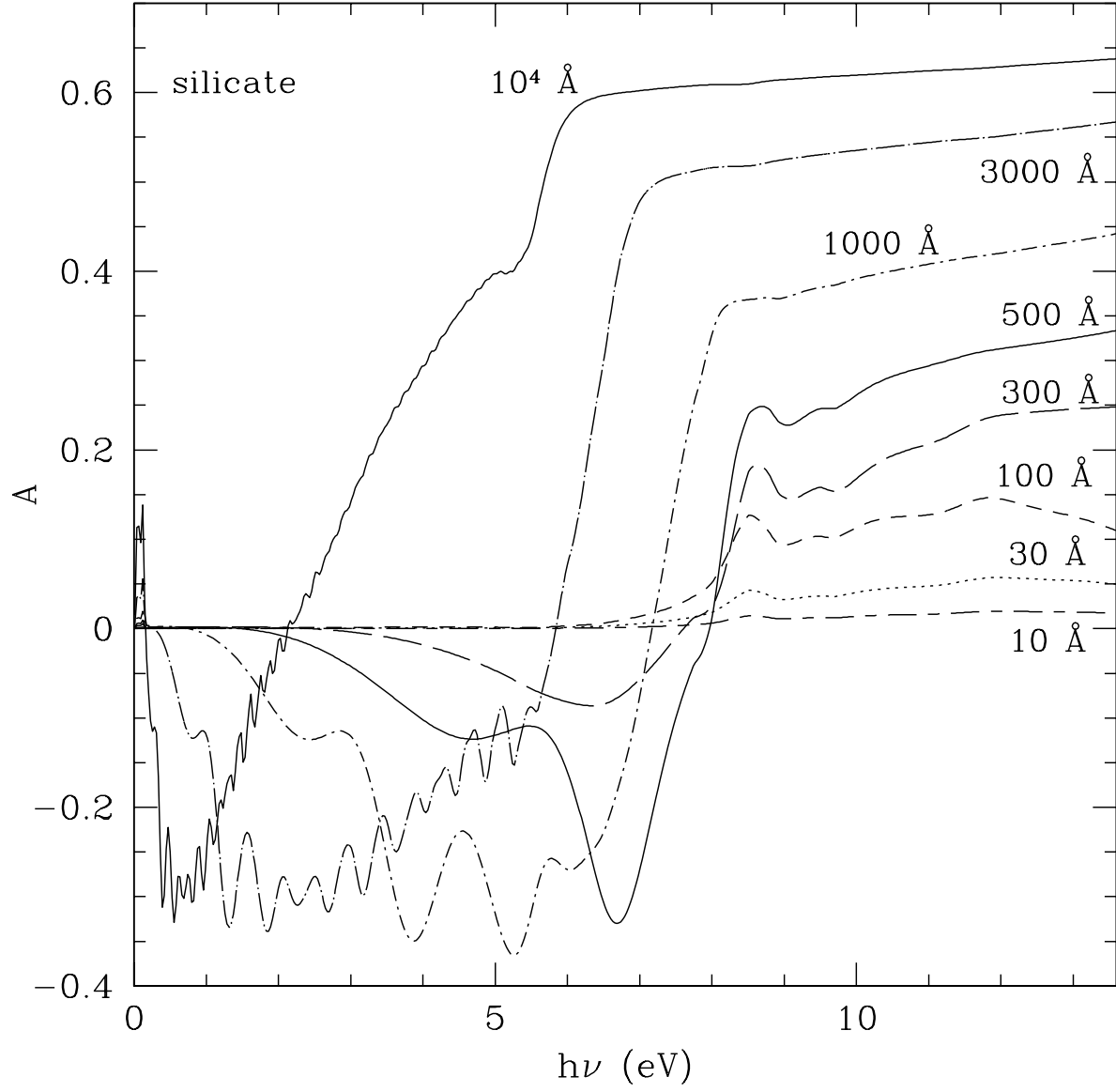


Fig. 7.— Same as Figure 6, but for silicate grains.

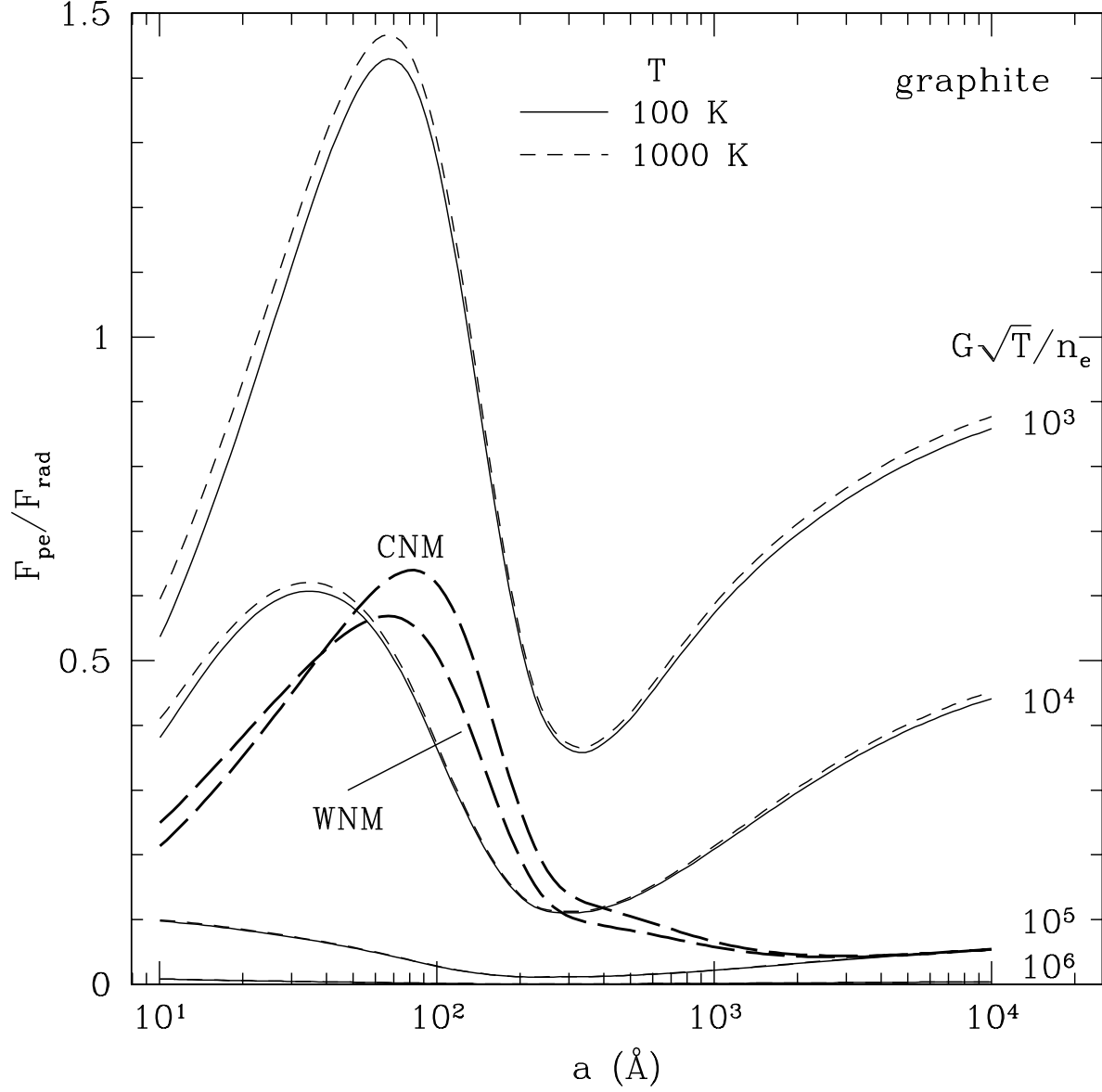


Fig. 8.— $F_{\text{pe}}/F_{\text{rad}}$ for graphite grains, $T_c = 3 \times 10^4$ K, and two gas temperatures: 100 K (solid) and 1000 K (dashed). The values of $G\sqrt{T}/n_e$, in $\text{K}^{1/2}\text{cm}^3$, are indicated. Curves labelled CNM (WNM) are for cold (warm) neutral media and the ISRF.

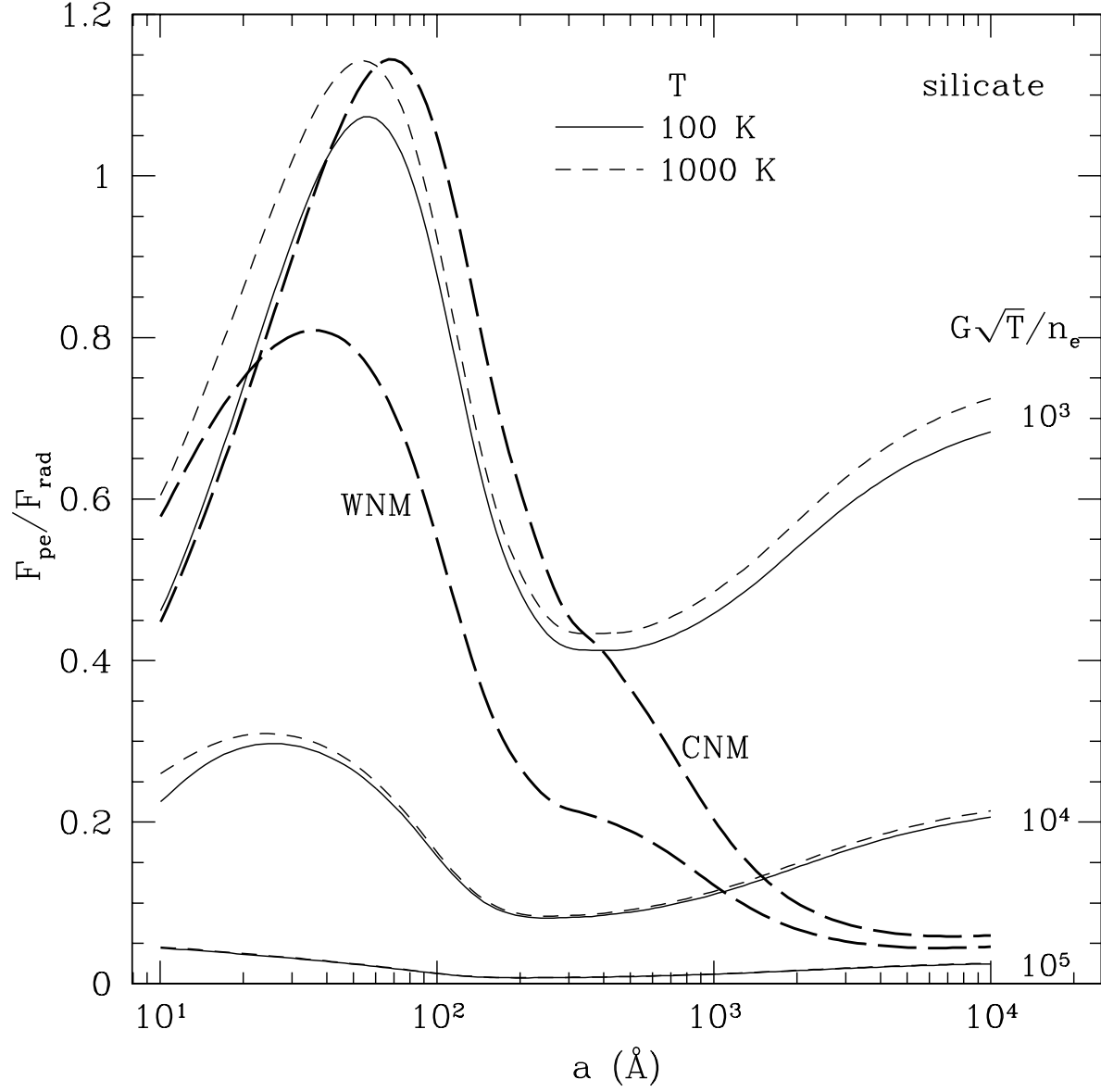


Fig. 9.— Same as Figure 8, but for silicate grains.

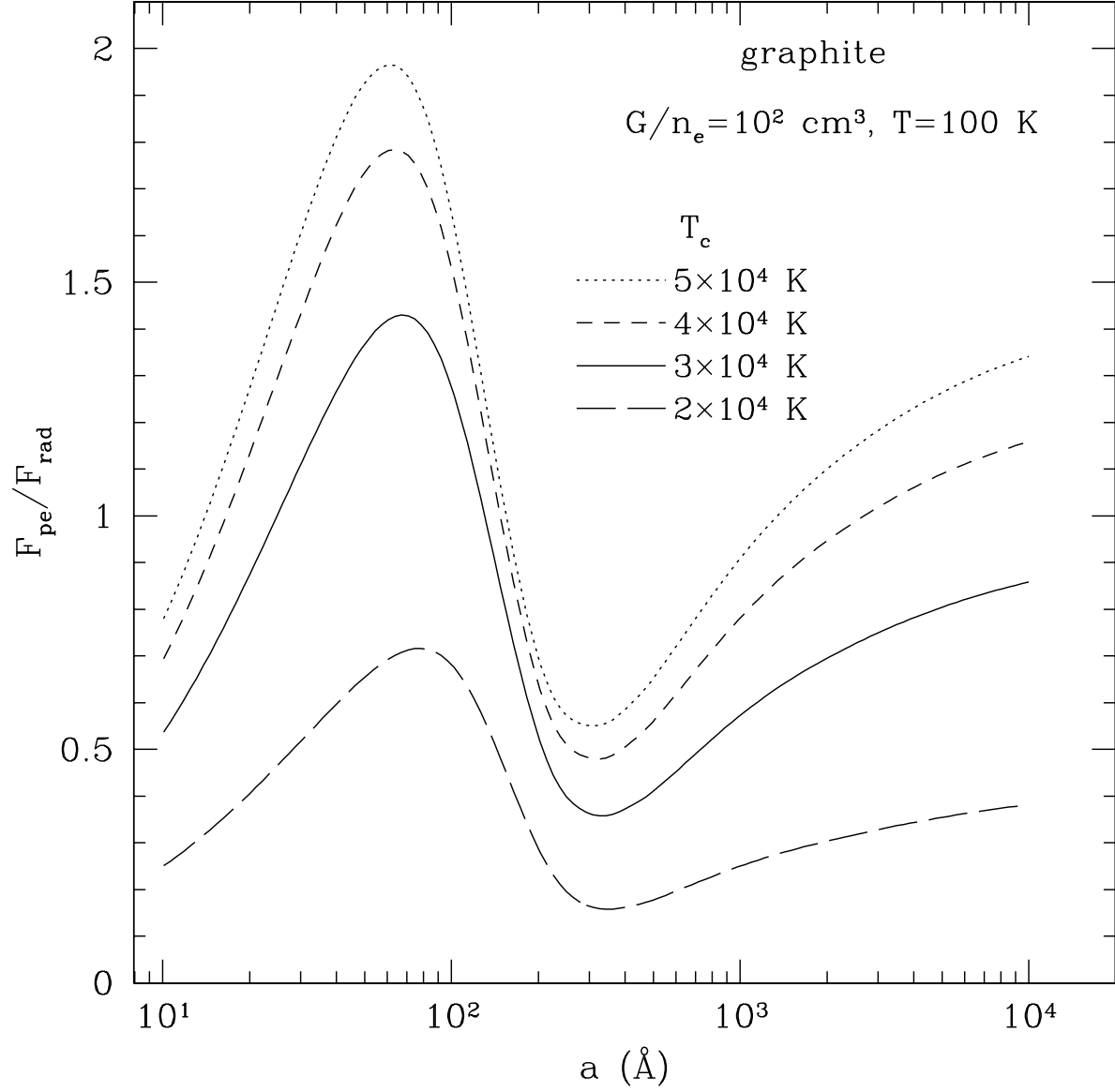


Fig. 10.— $F_{\text{pe}}/F_{\text{rad}}$ for graphite grains, $T = 100 \text{ K}$, $G\sqrt{T}/n_e = 10^3 \text{ K}^{1/2} \text{ cm}^3$, and four values of T_c as indicated.

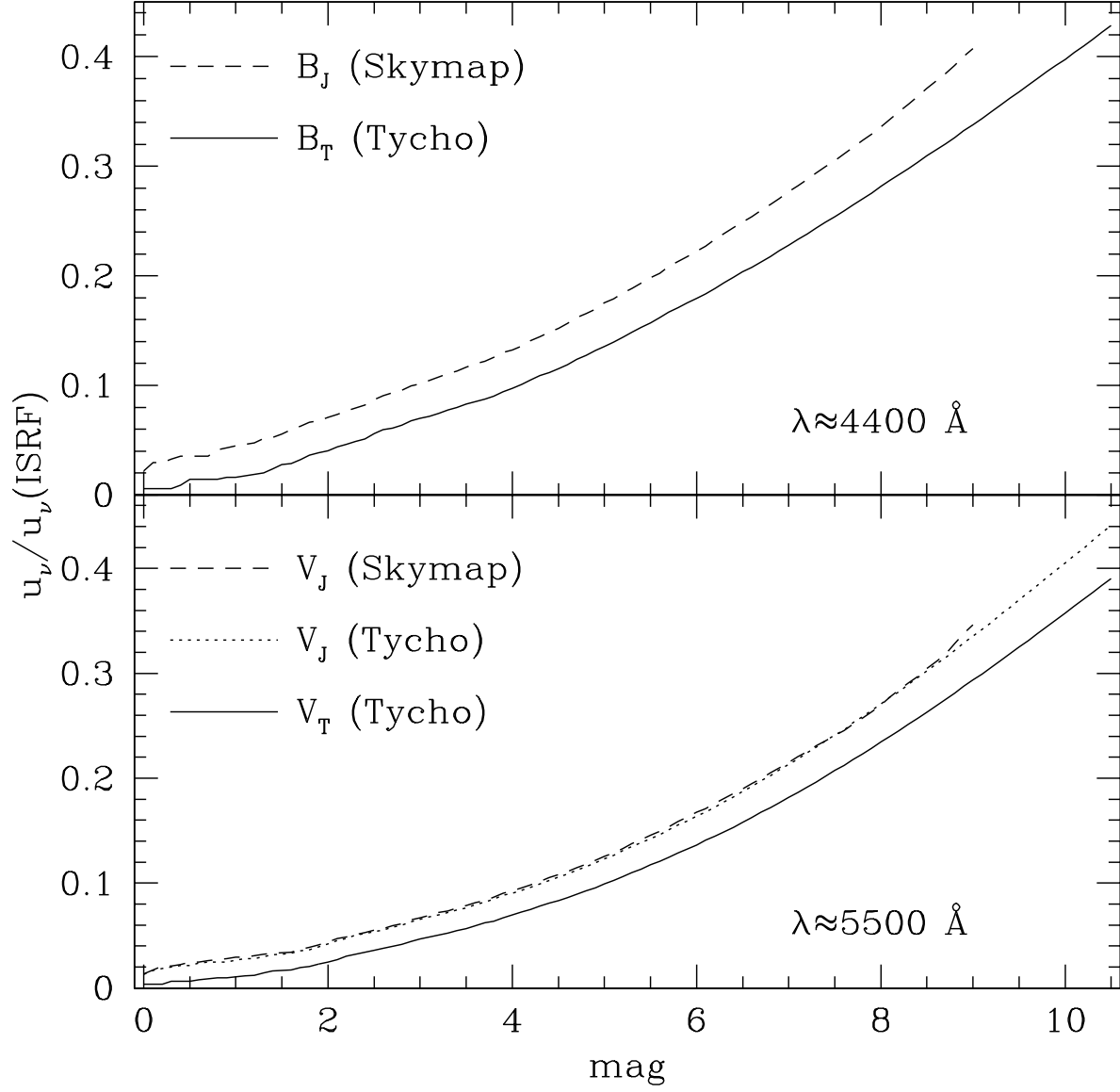


Fig. 11.— Energy density per wavelength interval, normalized to that of the ISRF (see eq 16), as a function of limiting magnitude. Results are from the Skymap and Tycho star catalogs. The Tycho fluxes are systematically low due to the absence of photometry for thousands of stars.

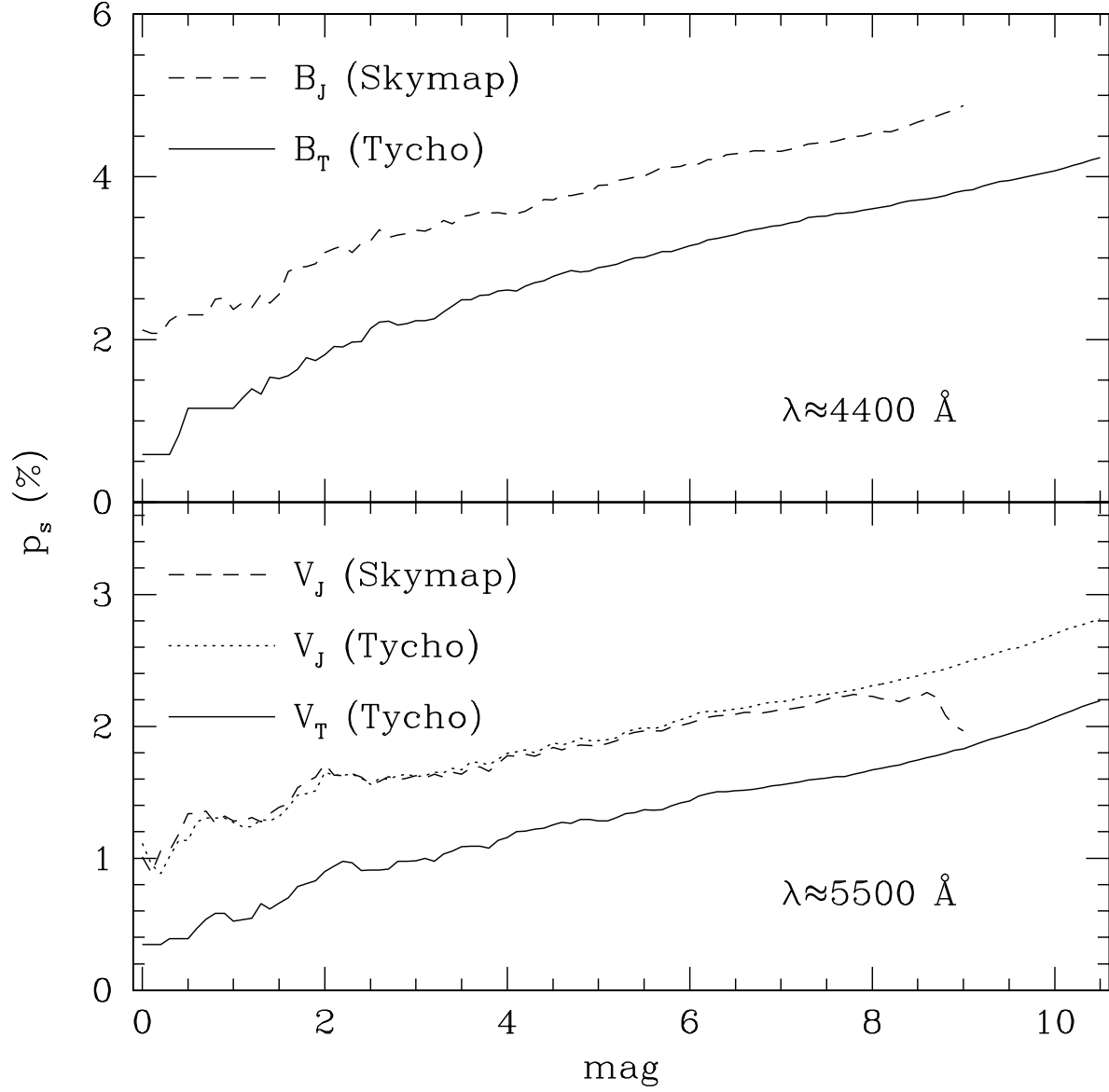


Fig. 12.— The normalized dipole moment p_s , i.e., the fraction of the energy density in the ISRF that is in the anisotropic component, as a function of limiting magnitude. The Tycho anisotropies are systematically low due to the absence of photometry for many of the brightest stars.

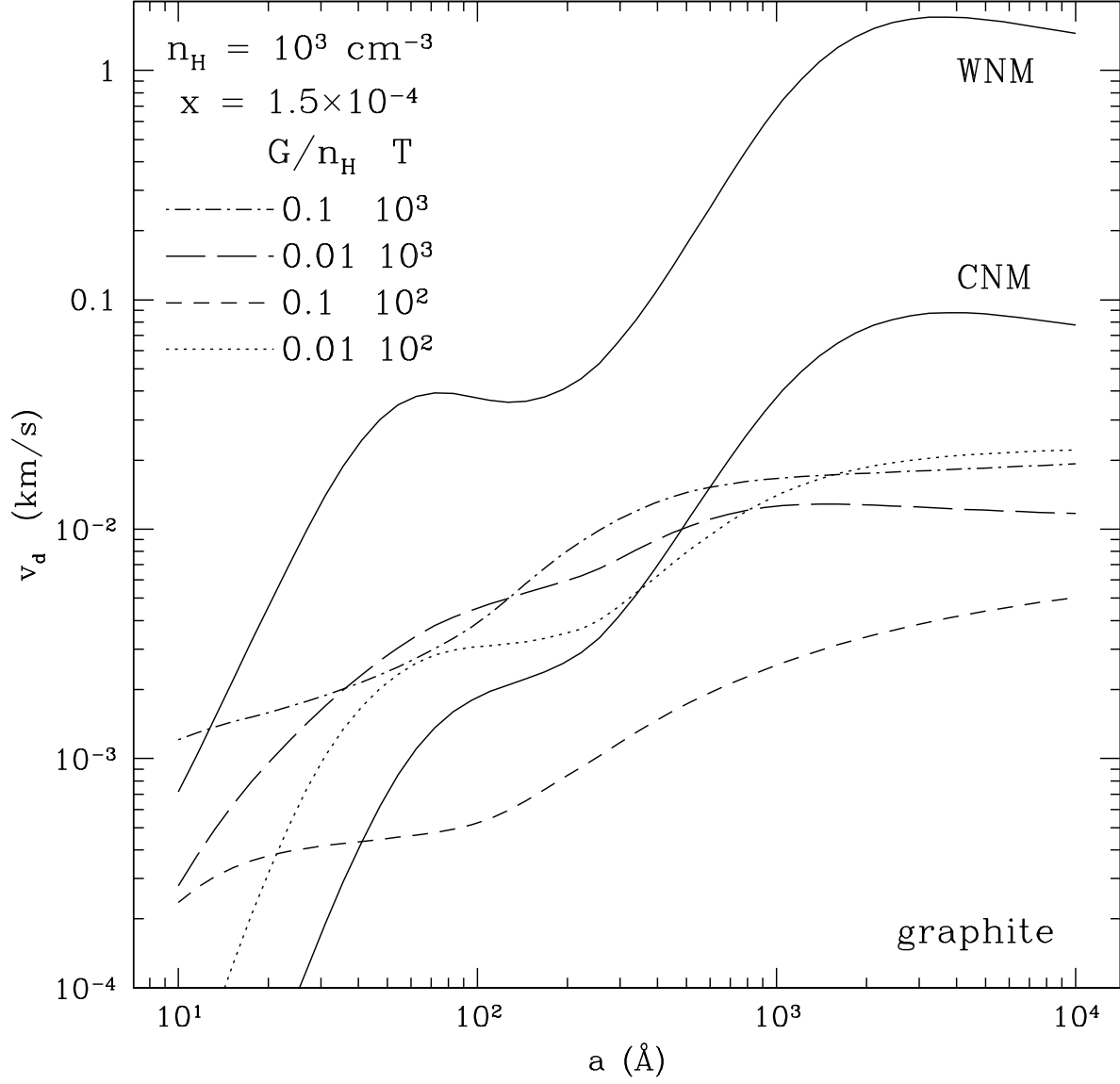


Fig. 13.— Drift speed v_d for graphite grains. Curves labelled CNM (WNM) are for cold (warm) neutral media, for an assumed anisotropy $\Delta u_{\text{rad}} = 0.1 u_{\text{rad}}$ in the ISRF. Anisotropies of this order are expected to be typical. The other curves are for locations where the radiation field is dominated by a single star or a cluster of stars, with $\Delta u_{\text{rad}} = u_{\text{rad}}$; the density is taken to be $n_{\text{H}} = 10^3 \text{ cm}^{-3}$ and the indicated values of G/n_{H} (T) are in cm^3 (K). For all cases we assume that the radiation anisotropy is parallel to the magnetic field; otherwise the drift velocity is modified according to equation (34).

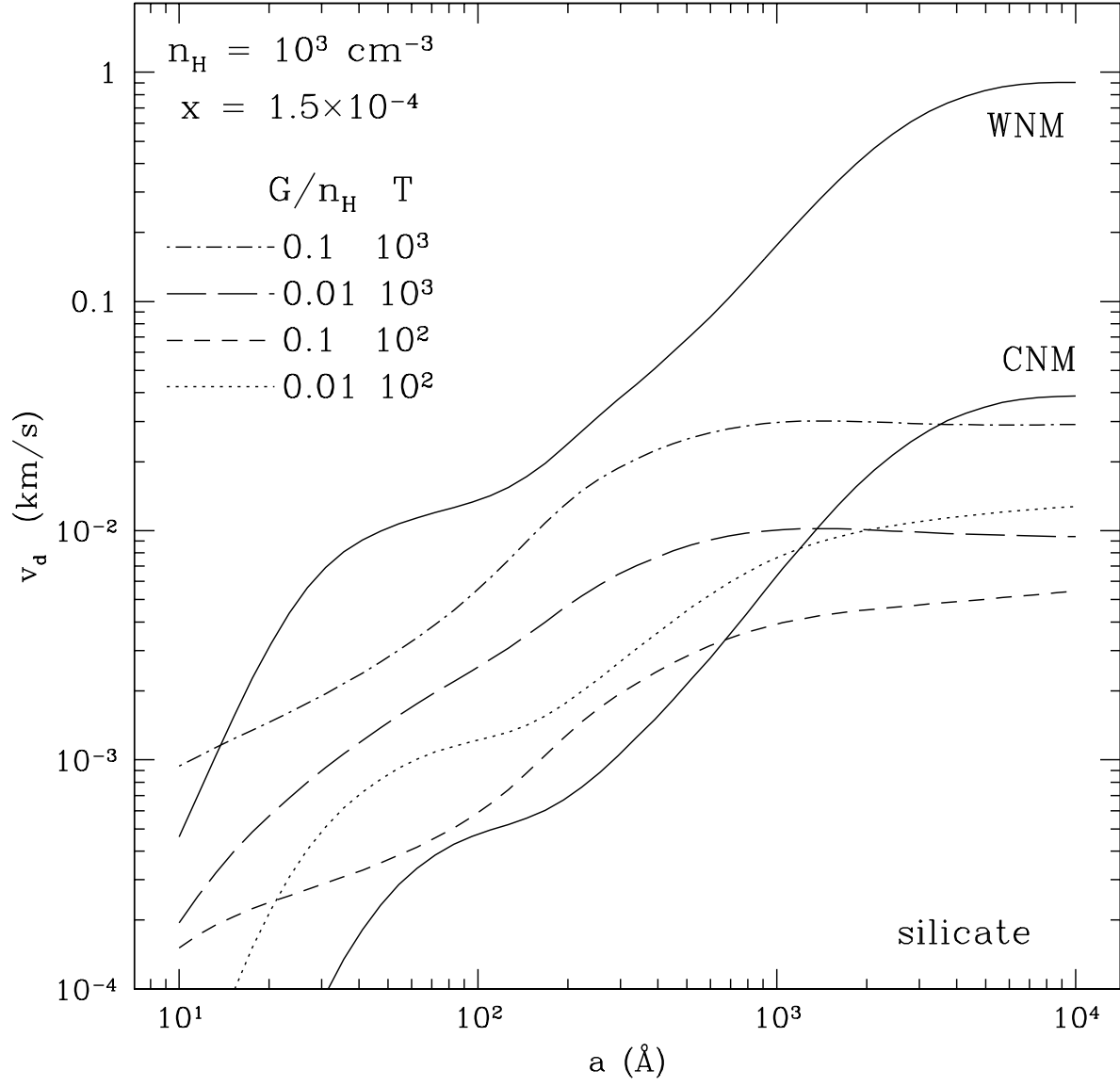


Fig. 14.— Same as Figure 13, but for silicate grains.

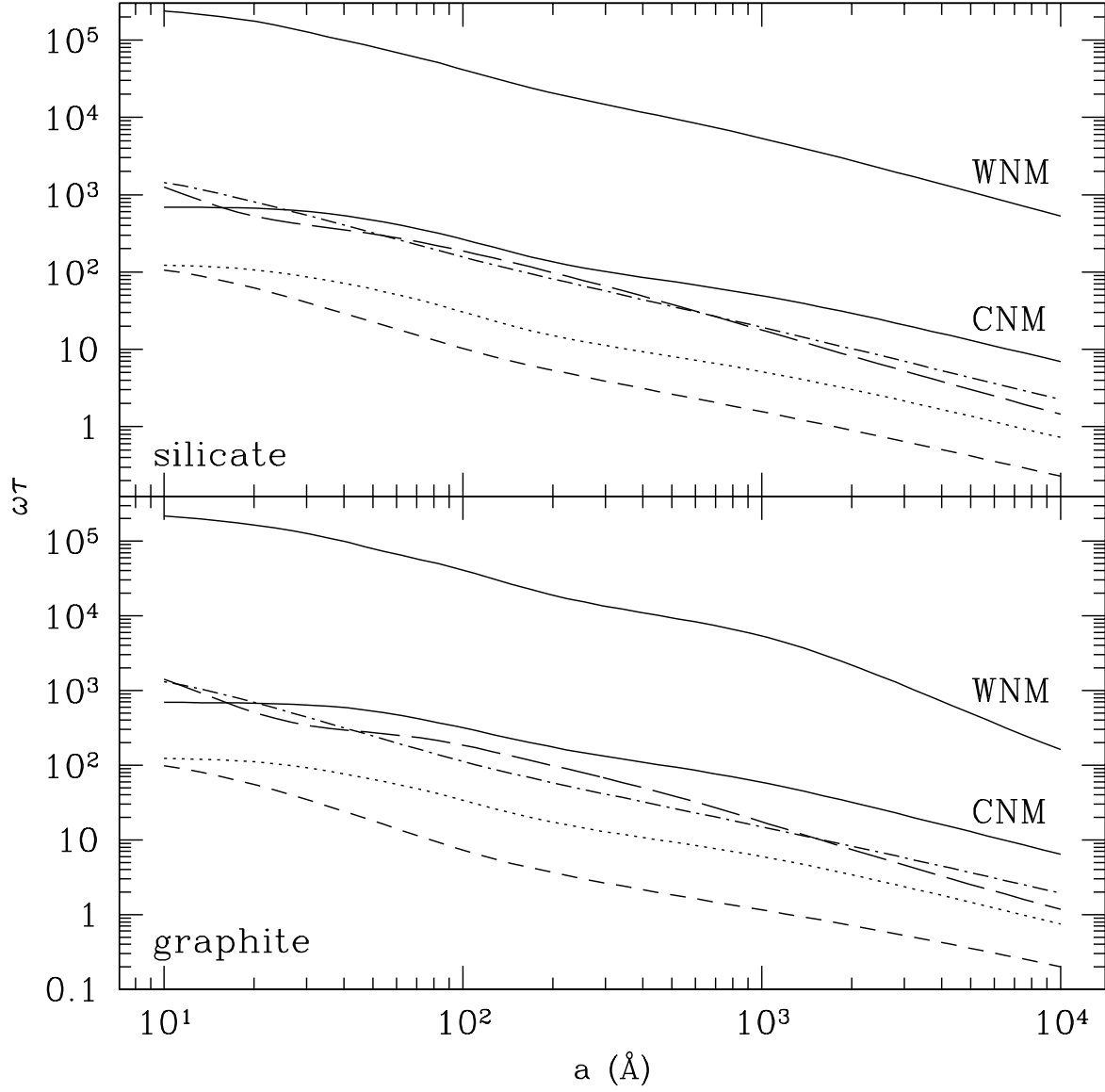


Fig. 15.— The product of the grain gyrofrequency ω and the gas-drag time, τ , for the same conditions as for the corresponding curves in Figures 13 and 14.

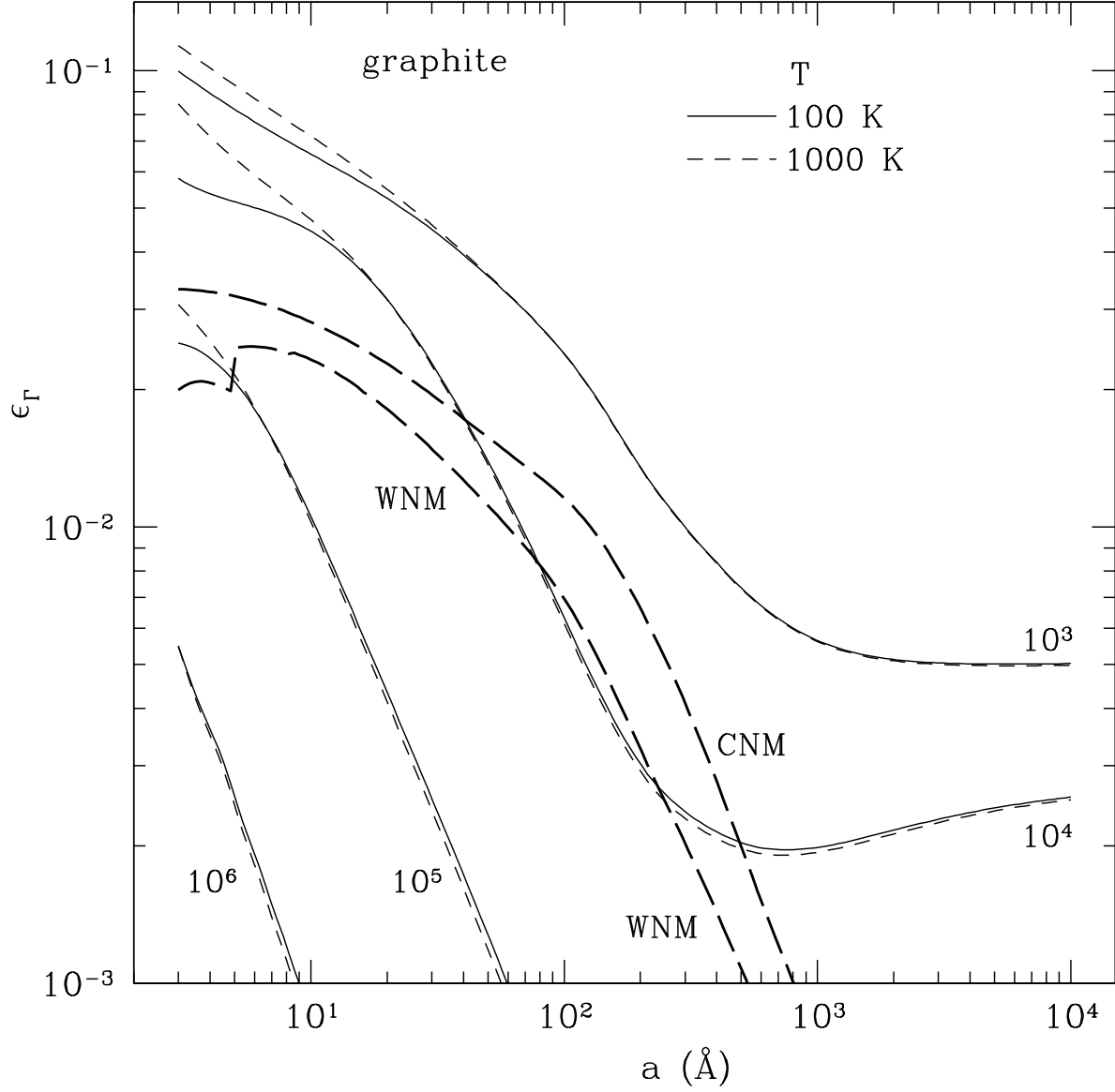


Fig. 16.— Gas heating efficiency for graphite grains for two gas temperatures: 100 K (solid) and 10³ K (short-dashed), four values of $G\sqrt{T}/n_e$, as labelled, and $T_c = 3 \times 10^4$ K. Curves labelled CNM (WNM) are for cold (warm) neutral media and the ISRF.

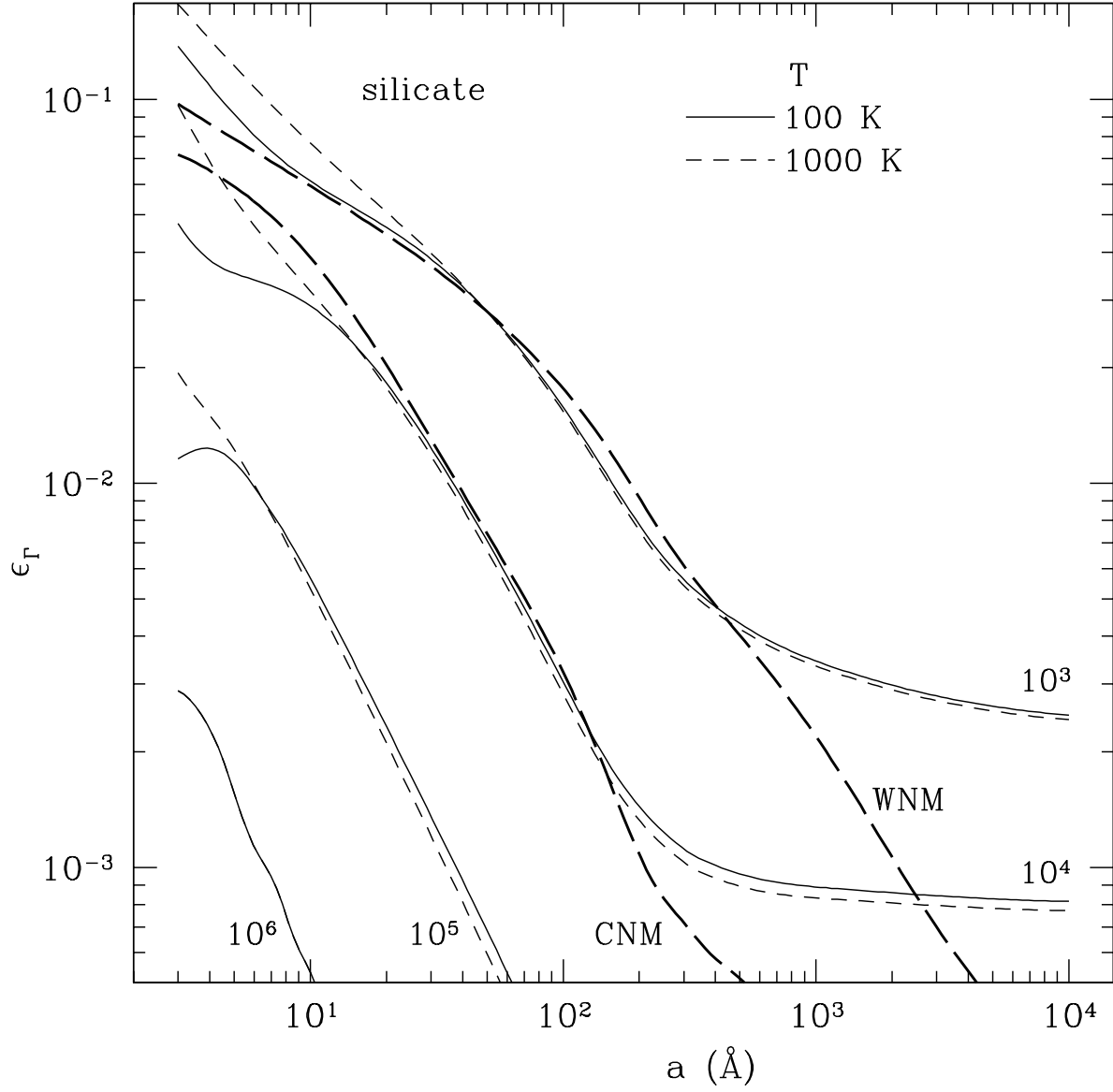


Fig. 17.— Same as Figure 16, but for silicate grains.

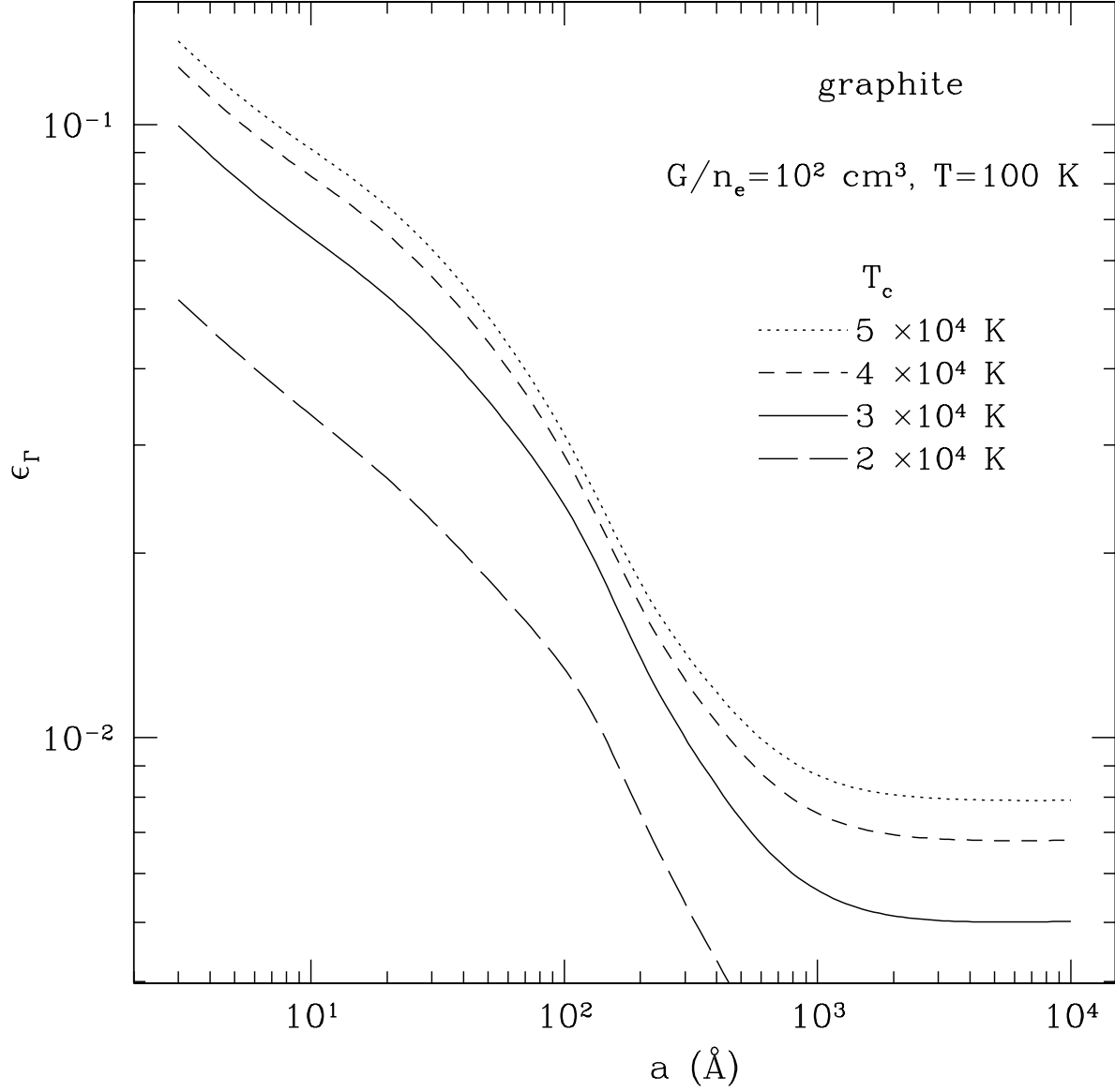


Fig. 18.— Gas heating efficiency for graphite grains, $T = 100 \text{ K}$, $G\sqrt{T}/n_e = 10^3 \text{ K}^{1/2} \text{ cm}^3$, and four values of T_c as indicated.

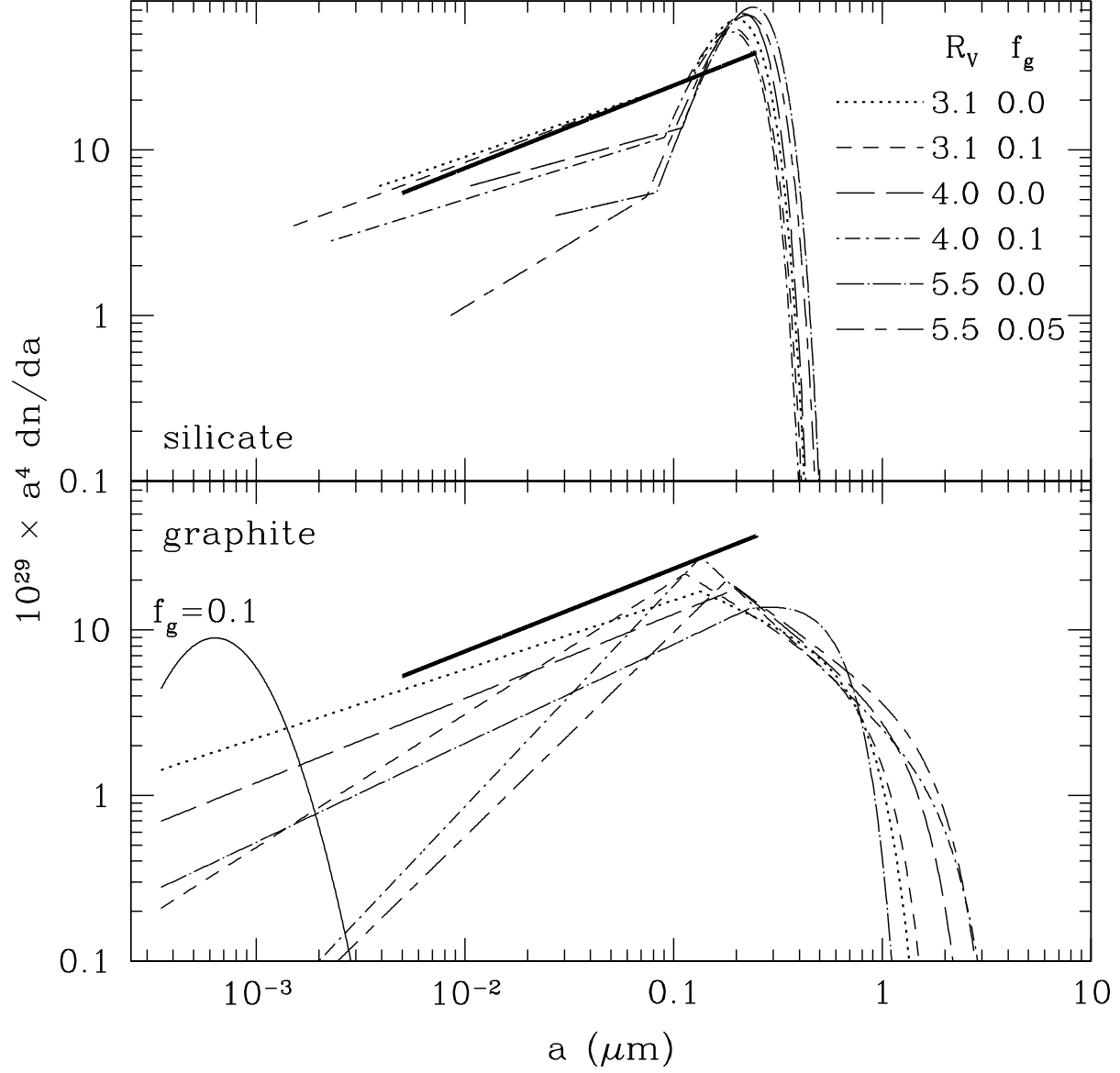


Fig. 19.— Grain size distributions obtained in Appendix A. The values of R_V , f_g are indicated. The log-normal graphite contribution is not included for each case; solid curve labelled $f_g = 0.1$ is for the log-normal population (eq. A2) with $f_g = 0.1$. The heavy, solid lines are the MRN distribution, for comparison.

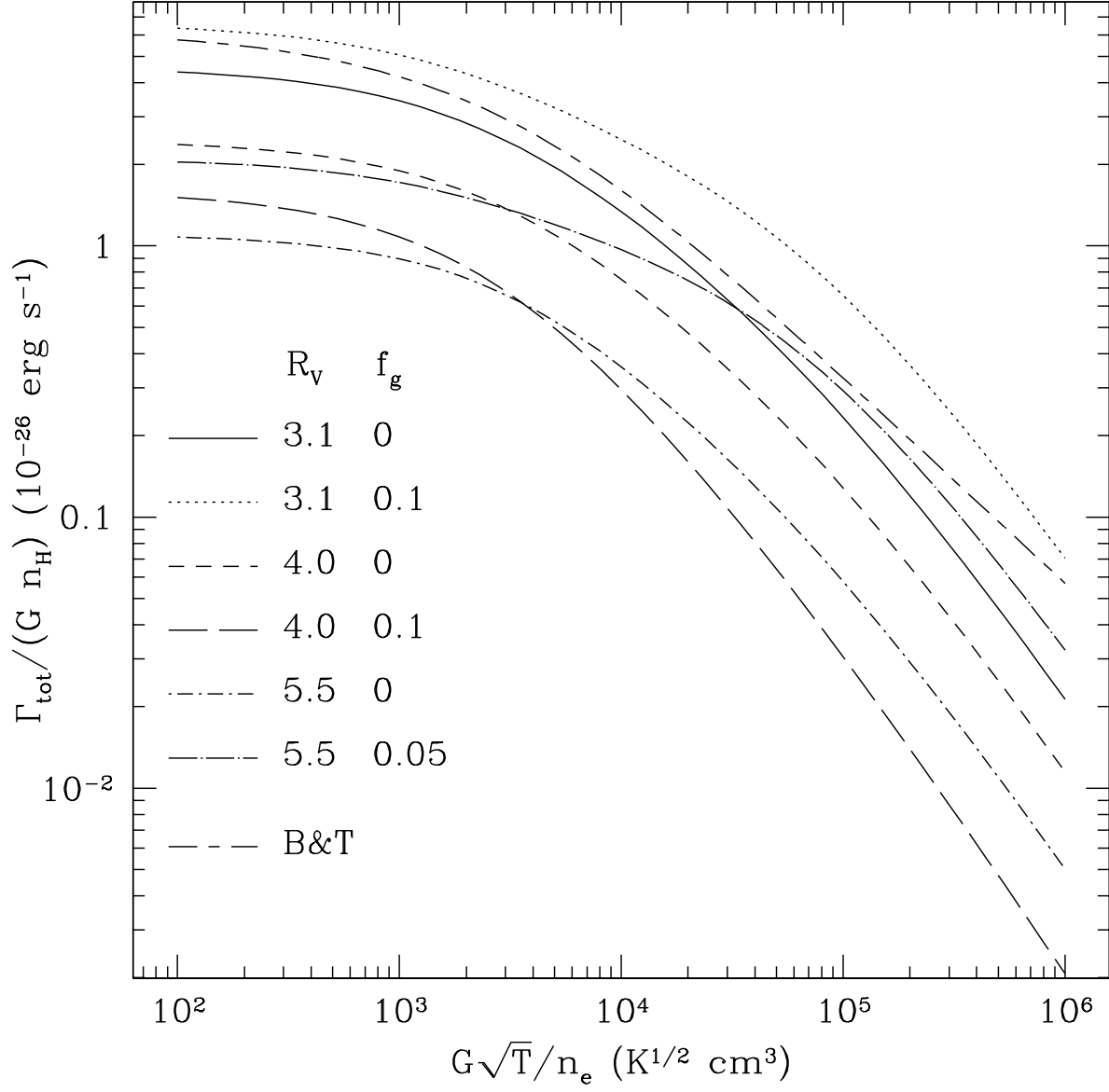


Fig. 20.— The photoelectric heating rate minus the cooling rate due to gas phase ions and electrons colliding with and sticking to the grains; for radiation color temperature of 3×10^4 K, gas temperature of 100 K, and graphite grain distributions derived in Appendix A for various values of R_V and f_g . For comparison, we also display the Bakes & Tielens (1994) result (B & T).

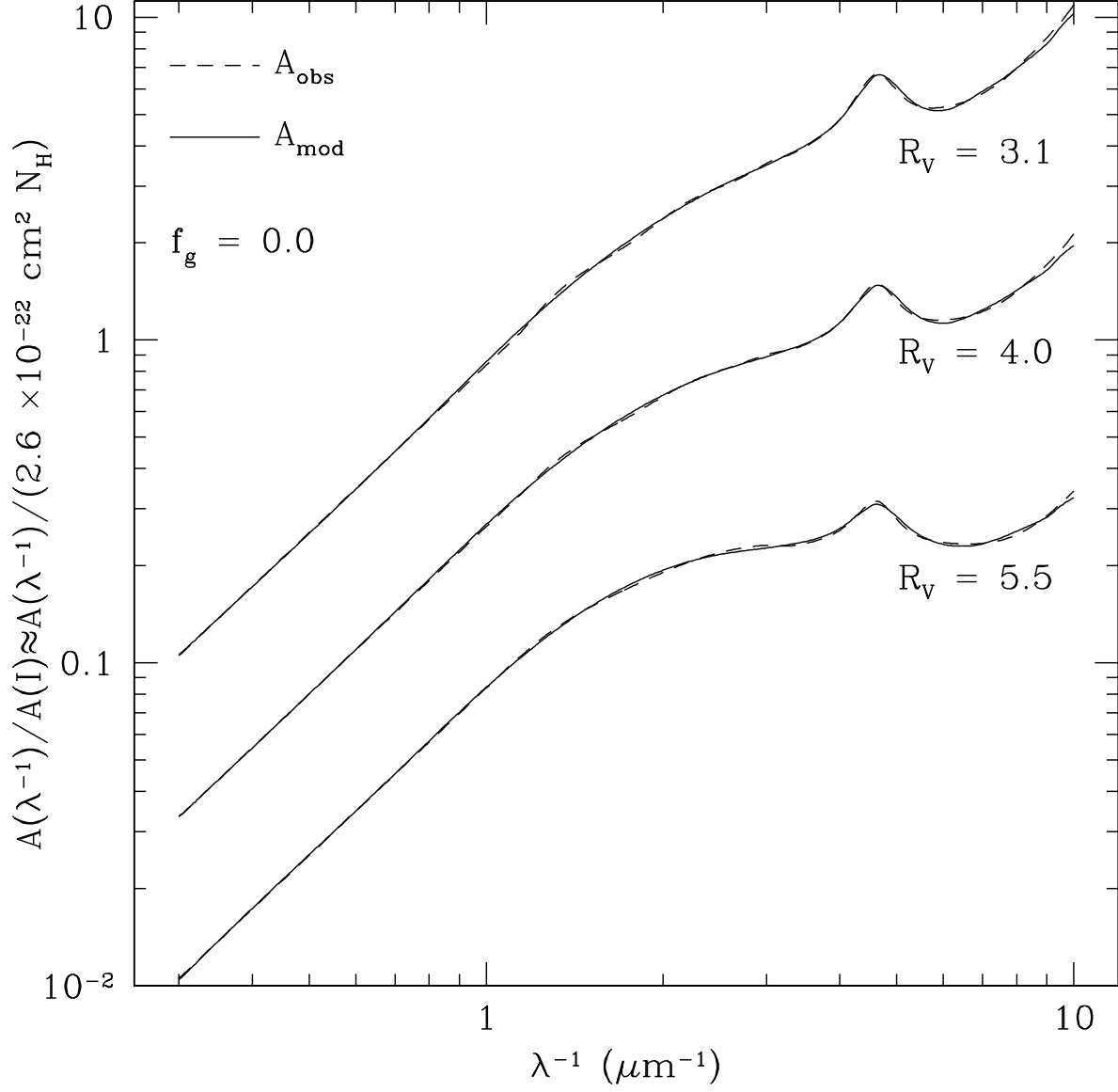


Fig. 21.— The average “observed” extinction A_{obs} and the extinction resulting from our models with $f_g = 0.0$. The curves for $R_V = 4.0$ (5.5) are scaled down by a factor $10^{0.5}$ (10), for clarity.

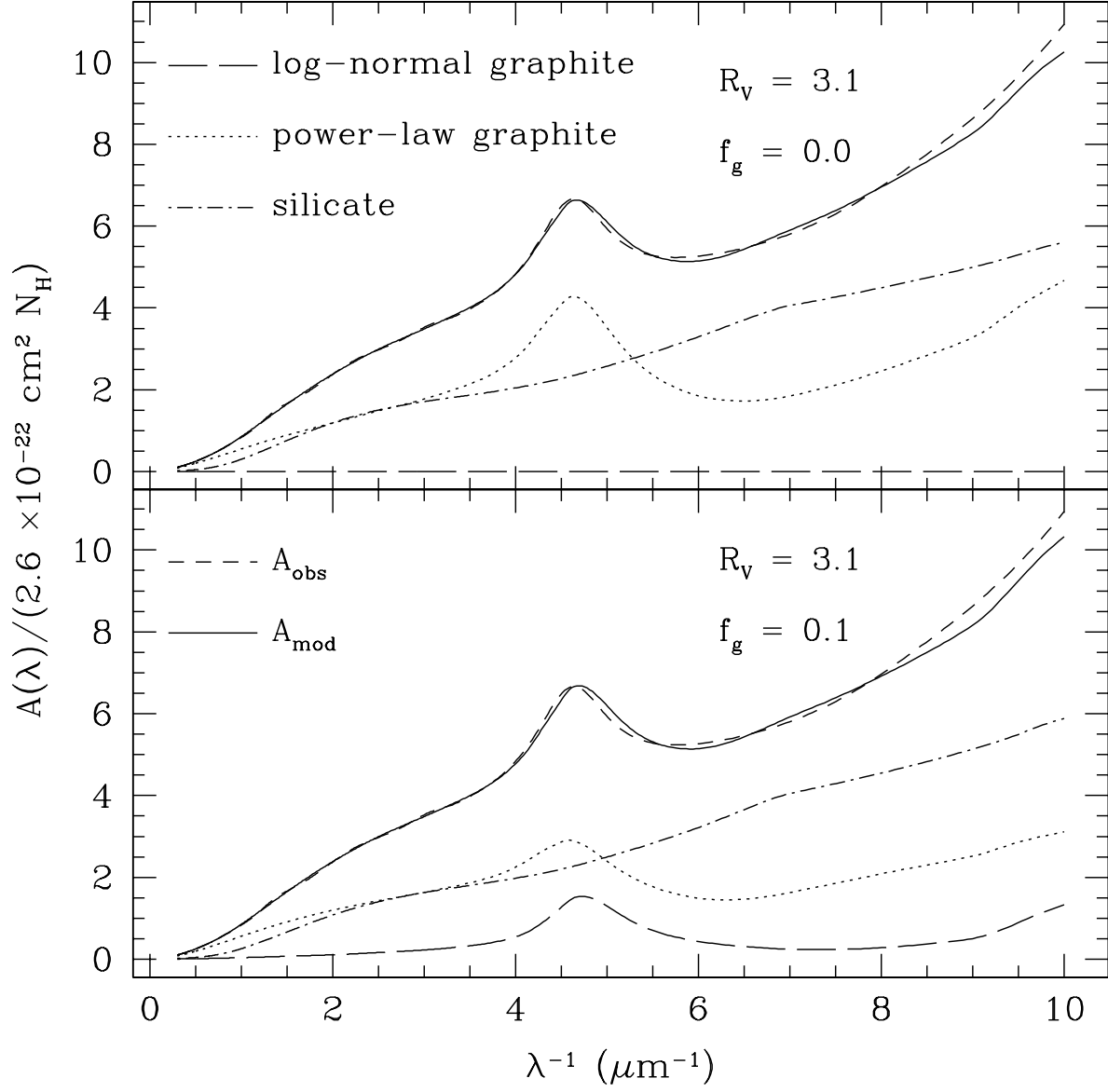


Fig. 22.— The extinction curve A_{mod} resulting from the grain distribution of equations A4 and A5, with parameters optimized to fit A_{obs} (see text) for $R_V = 3.1$ (also shown), for $f_g = 0.0$ and 0.1 . The contributions from the three grain distribution components are also shown.

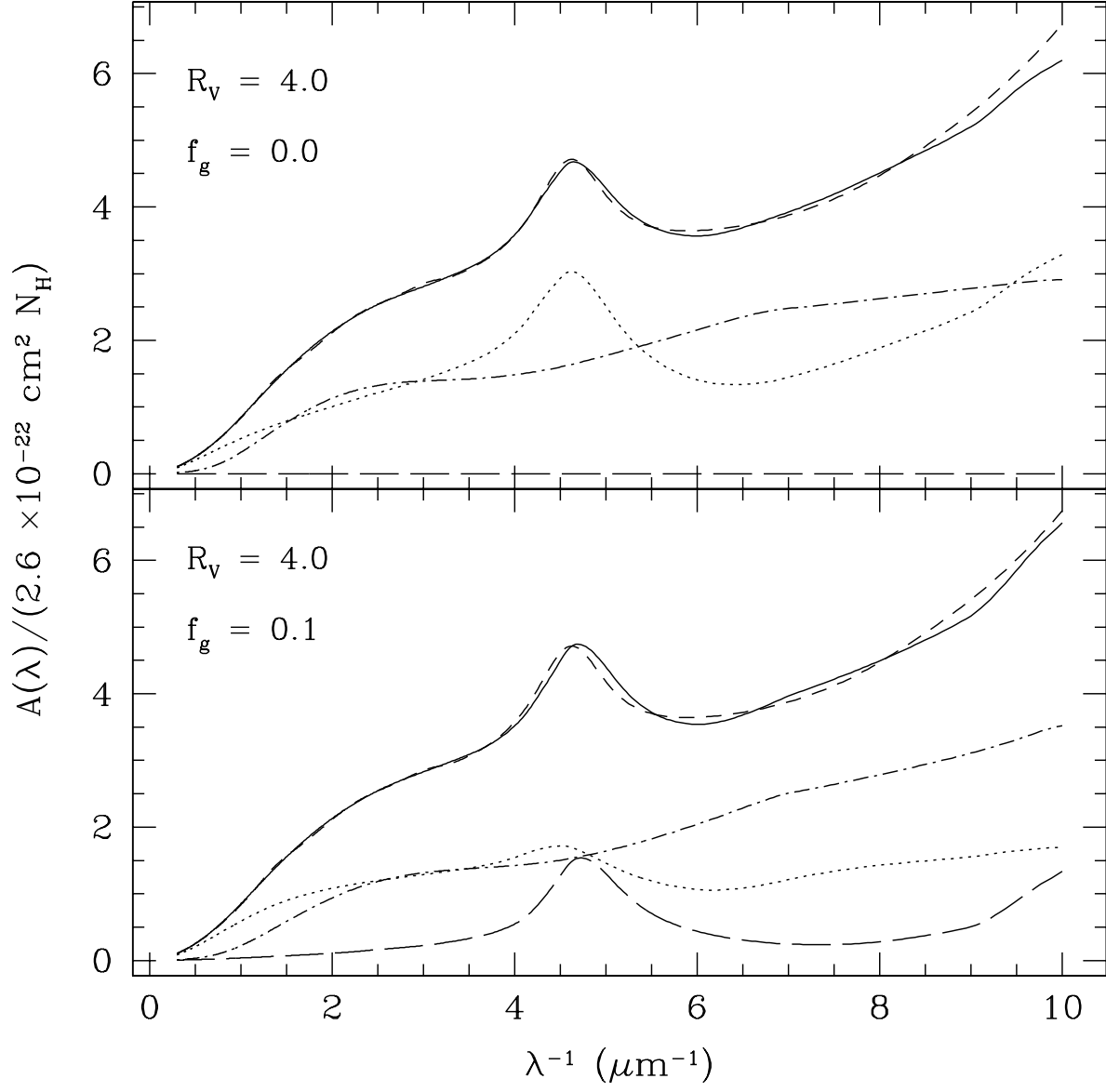


Fig. 23.— Same as Figure 22, but for $R_V = 4.0$ and $f_g = 0.0$ and 0.1 .

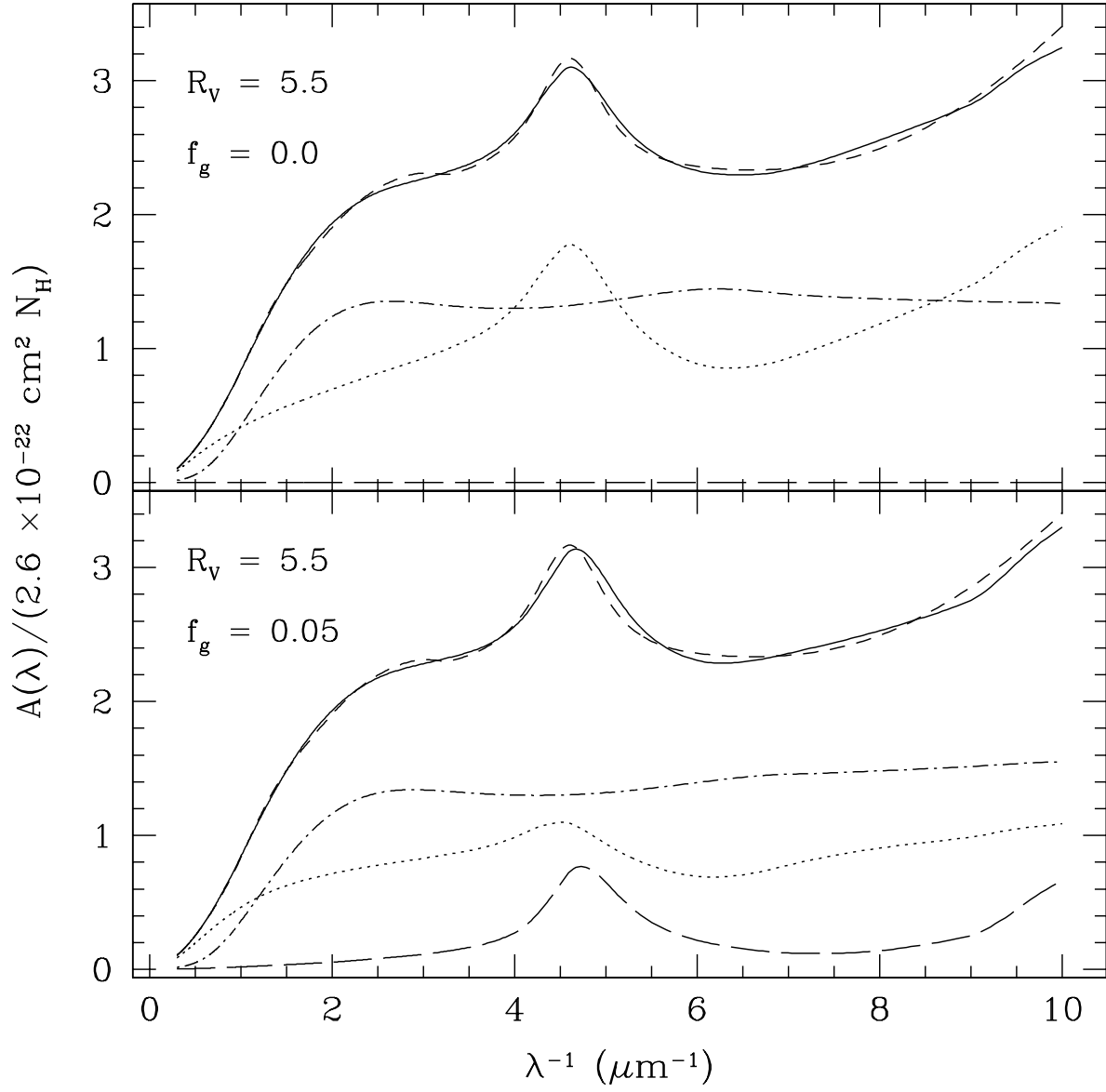


Fig. 24.— Same as Figure 22, but for $R_V = 5.5$ and $f_g = 0.0$ and 0.05 .

Table 1. Blackbody Components of the ISRF (Mathis et al. 1983)

i	W_i	T_i/K
1	10^{-14}	7500
2	1.65×10^{-13}	4000
3	4×10^{-13}	3000

Table 2. UV Energy Densities and Dipole Moments

Quantity	2740 Å	2365 Å	1965 Å	1565 Å
starlight dipole $(p_s \nu u_\nu)_*$ ^{a,b}	1.27	0.843	1.30	1.67
total starlight $(\nu u_\nu)_*$ ^{a,b}	4.43	3.23	4.73	5.27
total νu_ν ^{a,c}	4.90	5.47	6.47	6.90
ISRF νu_ν ^{a,d}	8.30	6.20	7.00	8.20
dipole/ISRF	0.152	0.136	0.185	0.205

^a $10^{-14} \text{ erg cm}^{-3}$

^bGondhalekar 1989

^cGondhalekar et al. 1980

^dfrom eq (16), Mathis et al. 1983

Table 3. Anisotropy Directions

Band	RA	dec	l	b
1565 Å	141°	−62°	281°	−8.2°
1965 Å	132°	−58°	275°	−8.9°
2365 Å	124°	−55°	270°	−10.5°
2740 Å	129°	−56°	273°	−9.3°
B	115°	−43°	257°	−9.8°
V	115°	−51°	264°	−13.6°

Note. — Celestial coordinates: right ascension (RA) and declination (dec); Galactic coordinates: longitude (l) and latitude (b).

Table 4. Photoelectric Heating Parameters;^a Part 1

R_V	f_g	rad field ^b	C_0	C_1	C_2	C_3
3.1	0.0	B0	5.61	1.43×10^{-3}	6.54×10^{-3}	5×10^{-4}
3.1	0.03	B0	6.11	3.34×10^{-3}	6.25×10^{-3}	3.37×10^{-4}
3.1	0.05	B0	7.11	5.81×10^{-3}	2.16×10^{-2}	3.62×10^{-4}
3.1	0.07	B0	6.73	7.72×10^{-3}	6×10^{-3}	3.5×10^{-4}
3.1	0.1	B0	7.65	1.18×10^{-2}	9.07×10^{-3}	2.3×10^{-4}
4.0	0.0	B0	3.11	6.52×10^{-4}	1.11×10^{-2}	1.64×10^{-4}
4.0	0.03	B0	3.59	3.21×10^{-3}	1.8×10^{-2}	4×10^{-4}
4.0	0.05	B0	3.85	5.79×10^{-3}	1.52×10^{-2}	1.93×10^{-4}
4.0	0.07	B0	4.26	8.89×10^{-3}	1.6×10^{-2}	1.99×10^{-4}
4.0	0.1	B0	4.85	1.43×10^{-2}	1.3×10^{-2}	2.02×10^{-4}
5.5	0.0	B0	1.25	2×10^{-4}	8.91×10^{-4}	3.41×10^{-4}
5.5	0.03	B0	1.66	3.47×10^{-3}	8.64×10^{-3}	2.49×10^{-4}
5.5	0.05	B0	2.26	7.76×10^{-3}	1.2×10^{-2}	1.43×10^{-4}
3.1	0.0	ISRF	4.06	1.38×10^{-3}	7.49×10^{-3}	6.11×10^{-4}
3.1	0.03	ISRF	4.45	3.38×10^{-3}	7.59×10^{-3}	6.33×10^{-5}
3.1	0.05	ISRF	4.58	5.51×10^{-3}	6.07×10^{-3}	2.52×10^{-4}
3.1	0.07	ISRF	4.81	7.98×10^{-3}	8.5×10^{-3}	5.49×10^{-5}
3.1	0.1	ISRF	5.19	1.28×10^{-2}	1.25×10^{-2}	7×10^{-5}

^aSee eq (40).

^bB0 refers to a blackbody spectrum with $T_c = 3 \times 10^4$ K and the ISRF of Mathis et al. (1983) is defined in eq (16).

Table 4. Photoelectric Heating Parameters, Part 2

C_4	C_5	C_6	err	h_s
0.82	0.654	0.66	0.17	0.61
0.747	0.643	0.668	0.16	0.67
0.709	0.5	0.72	0.17	0.71
0.675	0.614	0.674	0.16	0.74
0.647	0.571	0.711	0.16	0.77
0.83	0.6	0.76	0.16	0.51
0.691	0.496	0.718	0.13	0.64
0.639	0.497	0.762	0.14	0.70
0.609	0.474	0.77	0.16	0.76
0.575	0.474	0.773	0.17	0.82
0.857	0.857	0.59	0.15	0.52
0.602	0.513	0.75	0.14	0.71
0.556	0.486	0.784	0.15	0.79
0.794	0.623	0.639	0.16	0.58
0.717	0.625	0.762	0.17	0.65
0.677	0.623	0.67	0.18	0.68
0.641	0.577	0.792	0.17	0.71
0.603	0.521	0.798	0.17	0.74

Table 5. Recombination Cooling Parameters^a, Part 1

R_V	f_g	rad field ^b	D_0	D_1
3.1	0.0	B0	−11.	0.083
3.1	0.03	B0	−10.9	0.082
3.1	0.05	B0	−10.9	0.0814
3.1	0.07	B0	−10.8	0.0822
3.1	0.1	B0	−10.7	0.0804
4.0	0.0	B0	−11.6	0.0846
4.0	0.03	B0	−11.5	0.0826
4.0	0.05	B0	−11.4	0.0817
4.0	0.07	B0	−11.2	0.0804
4.0	0.1	B0	−11.1	0.0798
5.5	0.0	B0	−12.4	0.0848
5.5	0.03	B0	−12.1	0.082
5.5	0.05	B0	−11.9	0.0804
3.1	0.0	ISRF	−11.3	0.0593
3.1	0.03	ISRF	−11.2	0.0455
3.1	0.05	ISRF	−11.1	0.0394
3.1	0.07	ISRF	−11.0	0.034
3.1	0.1	ISRF	−10.9	0.0276

^aSee eq (41).

^bB0 refers to a blackbody spectrum with $T_c = 3 \times 10^4$ K and the ISRF of Mathis et al. (1983) is defined in eq (16).

Table 5. Recombination Cooling Parameters, Part 2

D_2	D_3	D_4	D_5	err
8.38	1.01	1.93	0.248	0.15
8.76	1.	2.09	0.246	0.15
8.93	0.999	2.16	0.243	0.17
9.1	0.996	2.23	0.242	0.2
9.28	0.988	2.28	0.24	0.21
8.5	1.	2.	0.252	0.15
9.12	0.993	2.27	0.248	0.2
9.32	0.985	2.33	0.242	0.23
9.44	0.981	2.34	0.24	0.25
9.62	0.977	2.39	0.234	0.28
8.52	0.998	1.93	0.245	0.15
9.61	0.979	2.42	0.241	0.28
9.84	0.968	2.47	0.233	0.32
7.83	0.962	1.69	0.199	0.2
7.43	0.925	1.53	0.168	0.23
7.16	0.896	1.48	0.153	0.25
6.79	0.867	1.45	0.141	0.25
5.95	0.827	1.43	0.127	0.26

Table 6. Photoelectric Heating Rates for H II Regions

R_V	f_g	T_c ^d	$\Gamma_{\text{pe}}/Gn_{\text{H}}$ ^{a,b}			$\Gamma_{\text{pe}}/Gn_{\text{H}}$ ^{a,c}		
			0.1 ^e	1.0	10.	0.1	1.0	10.
3.1	0.0	3.5	0.94	0.85	0.57	4.4	4.0	2.7
3.1	0.1	3.5	1.3	1.2	0.88	6.8	6.3	4.8
4.0	0.0	3.5	0.48	0.44	0.30	2.4	2.1	1.5
4.0	0.1	3.5	0.87	0.81	0.64	5.0	4.8	3.8
5.5	0.0	3.5	0.21	0.19	0.14	1.1	0.97	0.68
5.5	0.05	3.5	0.36	0.34	0.29	2.3	2.2	1.8
3.1	0.0	4.5	1.1	0.96	0.63	7.7	6.8	4.3
3.1	0.1	4.5	1.5	1.4	0.99	12.	11.	7.9
4.0	0.0	4.5	5.4	4.9	3.4	4.1	3.6	2.3
4.0	0.1	4.5	0.99	0.93	0.72	8.8	8.3	6.3
5.5	0.0	4.5	0.24	0.22	0.16	1.9	1.7	1.1
5.5	0.05	4.5	0.41	0.39	0.33	4.0	3.8	3.0

^a $10^{-25} \text{ erg s}^{-1}$

^bBlackbody spectrum cut off at 13.6 eV

^cFull blackbody spectrum

^d 10^4 K

^eValues for G/n_{H} , in cm^3

Table 7. Recombination Cooling Rates for H II Regions

R_V	f_g	T_c ^d	Λ/Gn_H ^{a,b}			Λ/Gn_H ^{a,c}		
			0.1 ^e	1.0	10.	0.1	1.0	10.
3.1	0.0	3.5	20.	2.3	0.44	21.	2.9	0.74
3.1	0.1	3.5	54.	5.8	0.86	55.	6.7	1.4
4.0	0.0	3.5	10.	1.2	0.22	10.6	1.5	0.34
4.0	0.1	3.5	47.	4.9	0.68	48.	5.6	1.1
5.5	0.0	3.5	4.5	0.52	0.099	4.7	0.67	0.18
5.5	0.05	3.5	23.	2.4	0.31	23.	2.6	0.51
3.1	0.0	4.5	20.	2.4	0.46	21.	3.4	0.96
3.1	0.1	4.5	54.	5.9	0.89	56.	7.4	1.8
4.0	0.0	4.5	10.	1.2	0.23	11.	1.8	0.50
4.0	0.1	4.5	47.	5.0	0.69	48.	6.1	1.4
5.5	0.0	4.5	4.5	0.53	0.10	4.9	0.79	0.23
5.5	0.05	4.5	23.	2.4	0.32	23.	2.9	0.66

^a $10^{-25} \text{ erg s}^{-1}$

^bBlackbody spectrum cut off at 13.6 eV

^cFull blackbody spectrum

^d 10^4 K

^eValues for G/n_H , in cm^3

Table 8. Grain Distribution Parameter Values for Extinction Fits, Part 1

R_V	f_g	α_g	$a_{t,g}$ (μm)	β_g	$a_{c,g}$ (μm)	C_g
3.1	0.0	−2.58	0.134	−3.56	0.860	7.03×10^{-14}
3.1	0.03	−2.49	0.125	−3.62	0.917	9.22×10^{-14}
3.1	0.05	−2.42	0.126	−3.72	1.05	9.44×10^{-14}
3.1	0.07	−2.37	0.127	−3.74	0.961	9.65×10^{-14}
3.1	0.1	−2.20	0.114	−3.78	1.00	1.49×10^{-13}
4.0	0.0	−2.49	0.202	−4.01	1.55	2.17×10^{-14}
4.0	0.03	−2.38	0.184	−3.88	1.21	2.90×10^{-14}
4.0	0.05	−2.30	0.181	−3.95	1.46	3.16×10^{-14}
4.0	0.07	−2.09	0.149	−3.88	1.51	6.19×10^{-14}
4.0	0.1	−1.67	0.135	−4.15	2.24	1.12×10^{-13}
5.5	0.0	−2.40	0.229	−2.71	0.632	1.11×10^{-14}
5.5	0.03	−2.12	0.222	−4.10	2.47	1.67×10^{-14}
5.5	0.05	−1.77	0.180	−3.93	1.99	3.43×10^{-14}

Table 8. Grain Distribution Parameter Values for Extinction Fits, Part 2

$a_{\min,s}$ (\AA)	α_s	$a_{t,s}$ (μm)	β_s	$a_{c,s}$ (μm)	C_s
38.9	−2.57	0.119	0.198	0.197	1.57×10^{-13}
25.9	−2.54	0.120	0.098	0.198	1.57×10^{-13}
15.6	−2.47	0.127	0.073	0.199	1.49×10^{-13}
15.0	−2.51	0.116	−0.062	0.196	1.75×10^{-13}
15.1	−2.53	0.116	−0.075	0.193	1.71×10^{-13}
106.	−2.66	0.110	1.09	0.195	1.02×10^{-13}
68.6	−2.55	0.105	0.573	0.202	1.23×10^{-13}
59.8	−2.60	0.094	0.077	0.211	1.54×10^{-13}
24.7	−2.50	0.089	−0.360	0.218	1.86×10^{-13}
22.9	−2.61	0.090	0.252	0.186	1.61×10^{-13}
271.	−2.71	0.083	0.462	0.229	9.78×10^{-14}
199.	−2.43	0.081	0.454	0.221	1.04×10^{-13}
85.5	−2.24	0.074	0.182	0.221	1.28×10^{-13}

Table 8. Grain Distribution Parameter Values for Extinction Fits, Part 3

\tilde{V}_g	\tilde{V}_s	χ_1^2	χ_2^2
0.873	1.37	0.014	0.027
0.882	1.37	0.014	0.027
0.880	1.38	0.015	0.034
0.889	1.37	0.016	0.031
0.913	1.33	0.018	0.034
0.755	1.03	0.010	0.024
0.746	1.06	0.011	0.023
0.746	1.08	0.012	0.023
0.763	1.07	0.013	0.025
0.828	0.960	0.018	0.029
0.560	0.969	0.012	0.017
0.609	0.921	0.013	0.021
0.618	0.915	0.015	0.021